

Spring 5-2017

Extended Surface Heat Transfer Coefficients via Endwall Temperature Measurements

Yogesh Pai
Embry-Riddle Aeronautical University

Follow this and additional works at: <https://commons.erau.edu/edt>



Part of the [Aerodynamics and Fluid Mechanics Commons](#)

Scholarly Commons Citation

Pai, Yogesh, "Extended Surface Heat Transfer Coefficients via Endwall Temperature Measurements" (2017). *Doctoral Dissertations and Master's Theses*. 345.
<https://commons.erau.edu/edt/345>

This Thesis - Open Access is brought to you for free and open access by Scholarly Commons. It has been accepted for inclusion in Doctoral Dissertations and Master's Theses by an authorized administrator of Scholarly Commons. For more information, please contact commons@erau.edu.

EXTENDED SURFACE HEAT TRANSFER COEFFICIENTS VIA ENDWALL
TEMPERATURE MEASUREMENTS

A Thesis

Submitted to the Faculty

of

Embry-Riddle Aeronautical University

by

Yogesh Pai

In Partial Fulfillment of the

Requirements for the Degree

of

Master of Science in Aerospace Engineering

May 2017

Embry-Riddle Aeronautical University

Daytona Beach, Florida

EXTENDED SURFACE HEAT TRANSFER COEFFICIENTS VIA ENDWALL
TEMPERATURE MEASUREMENTS

By

Yogesh Pai

A Thesis prepared under the direction of the candidate's committee chairman, Dr. Mark Ricklick, Department of Aerospace Engineering, and has been approved by the members of the thesis committee. It was submitted to the School of Graduate Studies and Research and was accepted in partial fulfillment of the requirements for the degree of Master of Science in Aerospace Engineering.

THESIS COMMITTEE



Chairman, Dr. Mark Ricklick



Member, Dr. John Gordon Leishman



Member, Dr. Sandra Boetcher



Graduate Program Coordinator, Dr. Magdy Attia

4.25.2017

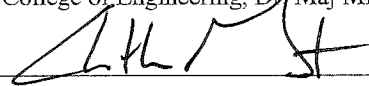
Date



Dean of College of Engineering, Dr. Maj Mirmirani

4/25/2017

Date



Vice Chancellor, Academic Support, Dr. Christopher Grant

4/25/2017

Date

ACKNOWLEDGMENTS

First and foremost, I would like to thank my committee members, Dr. Boetcher and Dr. Leishman for their valuable insights, suggestions and for being so kind to me. The entirety of this work has been possible due to my advisor Dr. Ricklick. Thank you for being so patient & constantly pushing me to strive harder. You've raised the bar for my future bosses and I can only wish that I can share half the rapport with them as I had with you. I can't begin to fathom the things you've done for me over the course of my Masters, you've been nothing but inspirational. I will always recall your mantra during arduous times, "If you knew what you were doing, it wouldn't be called research". I wouldn't even be here if not for my family. Thank you so much for always encouraging me to learn and giving me the opportunity to do so. I consider myself really lucky to have you guys as my support-system. I would like to thank my lab-mates; Royce, Anish, Bhushan, Yash, Sravan, Stanrich & Bianca for their support and critique. Their knowledge and insight is a major factor for the completion of my thesis. Also, I would like to make a special mention to Kiran, Johnny, Gopika, Chef Sundar, Jitesh, Amey, Sampu, Uday, OG Sundar, Nishu, Parth for all their support. I can't imagine life without you guys. I'm also indebted to ERAU for the infrastructure and financial support provided during my degree. I would have been crazier if it hadn't been for the active football community here in school. Daytona, you may not be the world's most famous beach but thanks for the awesome year-round sunny weather and the amazingly friendly people. You made me feel right at home. I would like to dedicate this work to my Ajja and Mauma, for I've not known a love truer than yours.

Thank you everyone for letting me be a part of something bigger. God bless you all and God bless the United States of America.

TABLE OF CONTENTS

SYMBOLS.....	vii
ABBREVIATIONS	viii
ABSTRACT.....	ix
1. Introduction.....	10
1.1 Motivation-The Need for Gas Turbine Cooling.....	10
1.2 Fundamentals of Heat Transfer & Extended Surfaces	13
1.3 Turbine Blade Cooling Methods	16
1.4 Pin-Fin Channel Flow Features.....	20
1.5 Experimental Measurement Techniques	22
2. Literature Review.....	24
3. Problem Statement	35
4. Methodology	37
4.1 Experimental Setup	37
4.2 Temperature Sensitive Paint	42
4.2 Data Reduction.....	44
4.2 CFD- Setup and Boundary Conditions	48
5. Extended Surface Methodology.....	51
5.1 Introduction to Extended Surface Analysis	51
5.2 Derivation of Analytical Solution.....	54
6. Results & Discussion	56
6.1 Analytical Verification Results.....	56
6.2 Computational Verification Results.....	59
6.3 Experimental Verification Results.....	59
6.3.1 Rig Validation- Intensity of Lights.....	60
6.3.2 Rig Validation- Heat Leakage Test	61
6.3.3 Rig Validation- Smooth Channel Test.....	62
6.3.4 Extended Surface Methodology Results-Comparison with Ames	64
6.3.5 Channel Average Nusselt number Results	66
7. Conclusion	70
REFERENCES	72

LIST OF FIGURES

Figure 1-1. Brayton cycle	10
Figure 1-2 Turbine inlet temperature versus Power (Sautner et al., 1992).....	11
Figure 1-3. Increase in turbine inlet temperature with various cooling methods over the years. (Clifford, 1985).....	12
Figure 1-4. Variety of Extended surfaces (Incropera & Dewitt, 2011)	15
Figure 1-5. Comparison of benefits of using extended surfaces with a flat surface.	16
Figure 1-6. Blade cooling techniques (Han, 2004).....	17
Figure 1-7. In-house pin-fin rig test section.....	18
Figure 1-8. Types of array arrangement: (a) Inline array (b) Staggered array (Siw et al., 2012).....	20
Figure 1-9. Flow features around a single cylinder. (Nguyen et al., 2012)	20
Figure 1-10. CFD simulation showcasing the flow features of a pin fin channel. (Fernandes, 2015)	21
Figure 2-1. Row averaged Nu for conducting and non-conducting pin arrays. (Metzger & Haley, 1982).....	26
Figure 2-2. Row averaged Sherwood numbers at pin surface & endwall for different Reynold's numbers. (Chyu, 1999).....	27
Figure 2-3. Midline Nu/Re ^{0.5} distribution of different rows for Re=30,000	29
Figure 2-4. Endwall Nusselt number contour for Re=13,000 for different streamwise spacings. (Lawson et al., 2011).....	30
Figure 2-5. Circumferential Frossling number distribution for different Re for cylindrical and oblong pins. (Kirsch et al., 2013).....	31
Figure 2-6. Cross section of pins tested. (Sahiti et el., 2006)	31
Figure 2-7. Array averaged Nu as a function of Re for different shapes.....	33
Figure 2-8. Array averaged Eu as a function of Re for different shapes.	33
Figure 2-9. Seal whisker and proposed bio-inspired cylinder.	34
Figure 2-10. Alternate geometries considered for the study. (Pai et al., 2017)	34
Figure 4-1. Experimental Setup.	37
Figure 4-2. Schematic of Flow Loop.....	40
Figure 4-3. Non-dimensional distances.....	41

Figure 4-3. Layout of the test section with boundary conditions.	40
Figure 4-4. Serpentine arrangement of Inconel strips in the test section.....	40
Figure 4-5. Circuit Diagram of the entire setup.	41
Figure 4-6. Jablonksi Diagram (Bell. 2001)	43
Figure 4-7. Typical TSP calibration curve (Fernandes, 2015).....	43
Figure 4-8. (a) Reference image of higher intensity, known temperature.	44
Figure 4-9. Pressure drop versus mass flow rate for the venturi-flowmeter.....	46
Figure 4-10. Boundary Conditions for the CHT case.	49
Figure 5-1. 2D Model of an extended surface.	51
Figure 5-2. Analytical Solutions for different tip conditions.....	53
Figure 6-1. Verification of Analytical solution w/ standard solution for infinite fin.	57
Figure 6-2. Temperature distribution along the pin height without IHG.....	60
Figure 6-3. Temperature distribution along the pin height with IHG.....	60
Figure 6-4. Intensity Stabilization over time	60
Figure 6-5. Schematic of Heat Leak Test arrangement	61
Figure 6-6. Heat Leakage Test Results- Difference in temperature vs Heat flux supplied.	62
Figure 6-7. Spanwise averaged smooth channel Nusselt number.....	63
Figure 6-8. Comparison of analytical solution with Ames for Re=3,000.....	64
Figure 6-9. Comparison of analytical solution with Ames for Re=10,000.....	65
Figure 6-10. Comparison of analytical solution with Ames for Re=30,000.....	66
Figure 6-11. Endwall Nusselt number contour Re=30,000.....	69
Figure 6-12. Comparison of average Nusselt numbers with previous research.	69

SYMBOLS

Greek

η	Isentropic efficiency
ρ	Specific resistivity. (Ohm/m)
μ	Dynamic viscosity. (Ns/m ²)
θ	Excess temperature function (K)
A_c	Cross-sectional area (m ²)
A_s	Surface area(m ²)
Bi	Biot number
C_p	Specific heat capacity
D	Pin diameter (m)
f	Darcy friction factor
D_h	Hydraulic diameter (m)
h	Heat transfer coefficient (W/m ² K)
H	Channel height (m)
I	Current supplied. (A)
k	Thermal conductivity of the pin (W/mK)
m	Fin parameter (m)
\dot{m}	Mass flow rate. (kg/s)
Nu	Nusselt number
Nu_0	Nusselt number for fully developed smooth channel flow
P	Perimeter (m)
p	Pressure (Pa)
Pr	Prandtl number
Q	Rate of heat transfer. (W)
q''_{lost}	Heat flux lost to the surrounding (W/m ²)
$q''_{supplied}$	Heat flux supplied (W/m ²)
q''_b	Heat flux supplied to the base(W/m ²)

\dot{q}	Internal heat generation(W/m^3)
R	Resistance of the strips. (Ohm)
Re	Reynolds number
T_b	Bulk temperature (K)
T_s	Surface temperature (K)
T_∞	Freestream temperature (K)
X	Streamwise distance (m)
Y	Spanwise distance (m)

ABBREVIATIONS

CFD	Computational Fluid Dynamics
CAD	Computer Aided Design
RANS	Reynolds Averaged Navier Stokes
LES	Large Eddy Simulation
DNS	Direct Numerical Solution
STAR-CCM+	Simulation of Turbulence in Arbitrary Regions-Computational Continuum Modeling
sCMOS	Scientific Complementary Metal-Oxide Semiconductor
TSP	Temperature Sensitive Paint
PSP	Pressure Sensitive Paint
IHG	Internal Heat Generation
CHT	Conjugate Heat Transfer
LED	Light Emitting Diode
ESM	Extended Surface Methodology
TBC	Thermal Barrier Coating
IR	Infrared
PTML	Propulsion Thermal Management Laboratory
PVC	Poly-vinyl Chloride
SST	Shear Stress Transport
UV	Ultraviolet
AC	Alternating Current

ABSTRACT

Pai, Yogesh MSAE, Embry-Riddle Aeronautical University, May 2017. Extended Surface Heat Transfer Coefficients via Endwall Temperature Measurements.

Short pins are used for internal cooling of the trailing edge in a gas turbine blade. A novel method is described in this thesis which helps in simplifying the experimental process used to obtain average heat transfer data on the pin surface, at the expense of additional post-processing complexity. The method is based on a unique, analytical solution of the longitudinal conduction equation with internal heat generation, allowing computation of heat transfer rates via pin base temperature measurements via Temperature Sensitive Paint, or similar non-intrusive methods. Verification of this method is done with comparisons to the solution of infinite fins with internal heat generation, conjugate computational results, and experimental data validated against the literature. Agreement within 8% of experimental and 2% of numerical results confirm the suitability of the method.

1. Introduction

1.1 Motivation-The Need for Gas Turbine Cooling

Most passenger aircrafts operating today are powered by gas turbine engines. Gas turbine engines are preferred for flight due to their high power-to-weight ratio as well as their robustness and efficiency in delivering power. High power output at maximum efficiency is one of the major requirements for engine manufacturers and designers as this helps in reducing fuel usage and ultimately operating costs for airlines. The Brayton cycle describes the working of a gas turbine engine as shown in Figure 1-1.

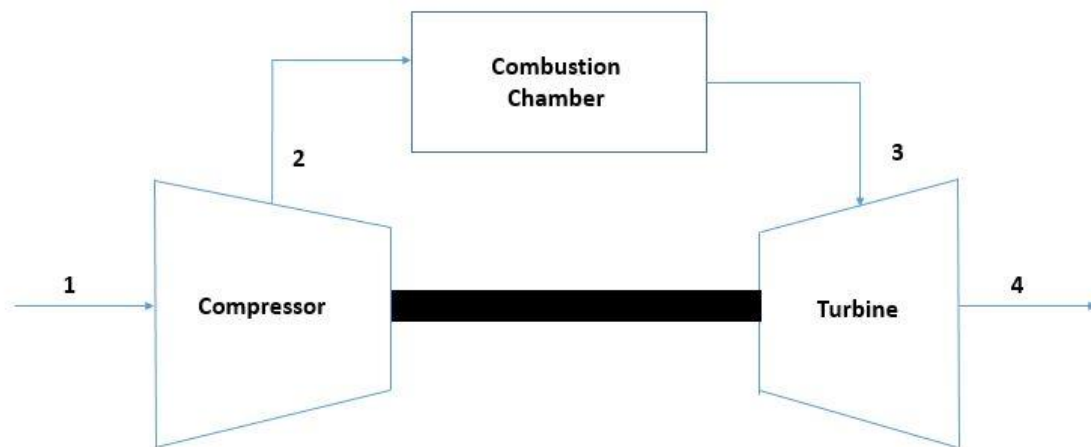


Figure 1-1. Brayton cycle

An ideal Brayton cycle consists of adiabatic compression in the compressor section (1-2), constant pressure heat addition in the combustor (2-3) and the last step in the process, expansion for energy extraction in the turbine section (3-4). The energy obtained from the turbine drives the compressor in this process. In simpler words, freestream air is

compressed in the compressor section and introduced in the combustor where fuel is added to this compressed air and ignited. This mixture of hot gas is then introduced into the turbine section where the turbine blades extract energy.

The isentropic efficiency of a gas turbine engine is given by:

$$\eta = 1 - \frac{T_4}{T_3} \quad (1)$$

where T_3 = Turbine Inlet Temperature

T_4 = Turbine Exit Temperature

Thus, from the above equation we can see that an increase in turbine inlet temperature results in an increase in the efficiency of a gas turbine engine. Figure 1-2 shows the increase in engine power for various engines with a corresponding increase in turbine inlet temperature.

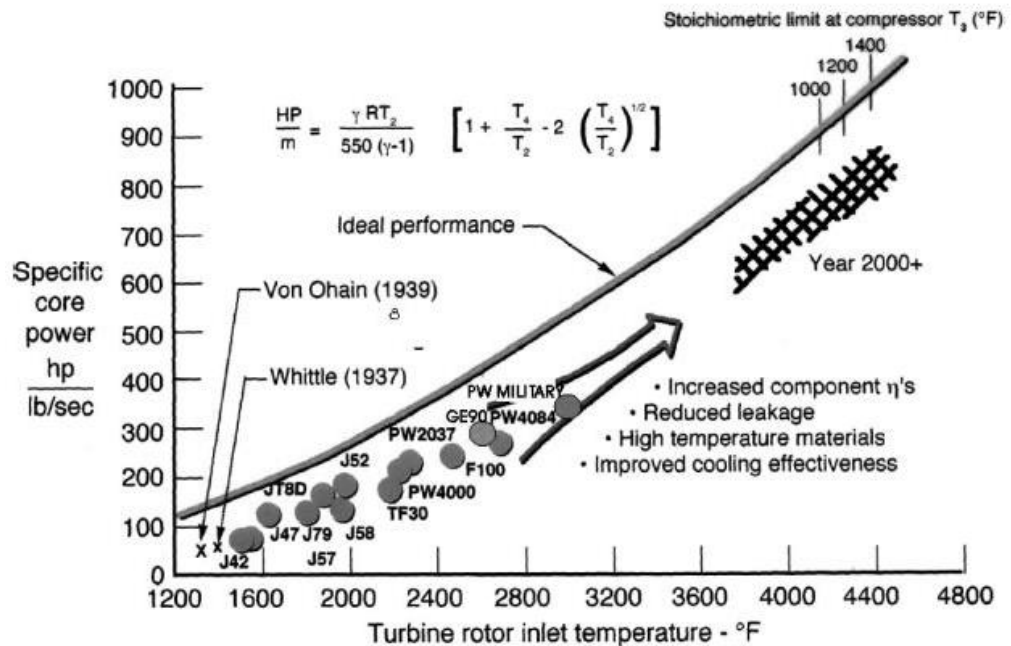


Figure 1-2 Turbine inlet temperature versus Power (Sautner et al., 1992)

Thus, increasing the turbine inlet temperature not only increases the efficiency but

also the power output as shown in Figure 1-2. However, the turbine inlet temperature is physically limited by the blade material limits. The hot blade component begins to weaken at a lower temperature as compared to blade material melting point (Han, 2004). This further limits the operating turbine inlet temperature with a view to promote component life. Hence, to allow hot gas temperatures beyond these limits, modern gas turbine blade components are either given thermal protective coatings, cooled or even both. Thermal barrier coatings (TBC) are used to minimize the effect of thermal stresses induced and reflect much of the radiant heat from the hot gases to prevent it from reaching the blade material. In addition to this, TBC's must retain its protective properties for prolonged service times and thermal cycles without failure (Clarke et al., 2012). TBCs are ceramics, based on Zirconium Dioxide–Yttrium Oxide and produced by plasma spraying (Muktinutalapati, 2011). Figure 1-3 shows the increase in turbine inlet temperature over the years with the introduction of various cooling techniques.

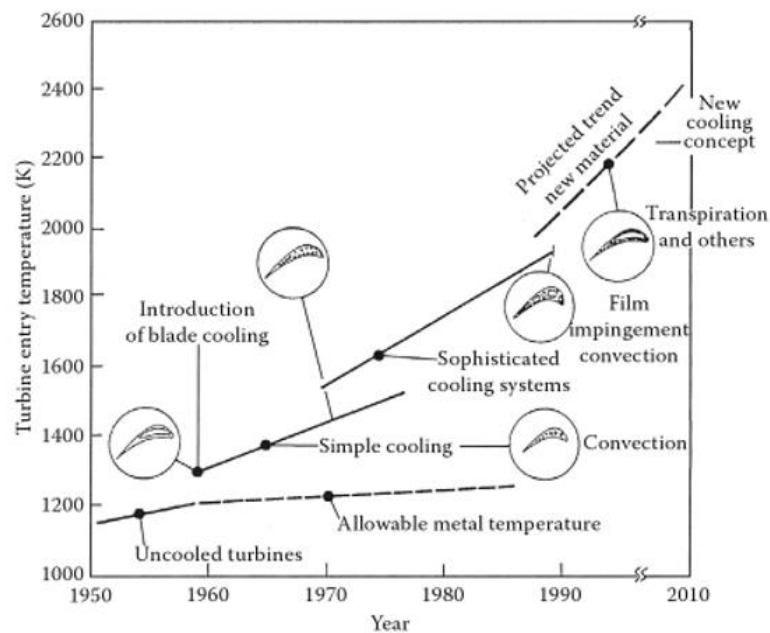


Figure 1-3. Increase in turbine inlet temperature with various cooling methods over the years. (Clifford, 1985)

From Figure 1-3, in the beginning, gas turbine engines without any cooling technologies were in use, which severely limited its efficiency. However, with the advent of cooling techniques starting from simple radial holes based convection cooling to sophisticated cooling techniques such as impingement, film cooling, pin-fins, rib cooling etc., the turbine inlet temperature ceiling was raised.

However, increased operating temperatures translate to increased thermal stresses on the blade. Thus, blade cooling along with a TBC on a gas turbine blade, made from a Nickel superalloy which could be either single crystal or directionally strengthened, whose melting point is already of the order of 1300°C (Gavrieli et al., 2004) is the answer to the requirements of modern day gas turbine engine. When TBC is used on these superalloy blades, the turbine inlet temperature ceiling can be pushed further up to 150°C above their customary limit (Muktinutalapati, 2011).

Thus, blade cooling techniques in conjunction with material advancement have helped increase the turbine inlet temperature over the years. Quantitatively speaking, over the past 50 years, materials advancement has helped increase turbine inlet temperatures at the rate of $4^{\circ}\text{C}/\text{year}(195^{\circ}\text{C})$ while it is $11^{\circ}\text{C}/\text{year}(525^{\circ}\text{C})$ due to the use of cooling techniques over the same time period (Boyce, 2006).

1.2 Fundamentals of Heat Transfer & Extended Surfaces

Before we delve into the different types of methods used in gas turbine cooling, we must try and understand the fundamentals of heat transfer and cooling. There are three primary modes of heat transfer; conduction, convection & radiation. The first two modes

are discussed in detail here since the focus of this thesis primarily deals with these.

Conduction may be viewed as the transfer of energy from the more energetic to the less energetic particles of a substance due to interactions between the particles. In simpler words, it can be defined as the transfer of heat between the hot surface and the colder surface, which are in physical contact with each other, because of the existing temperature gradient between them. The rate of conduction heat transfer is given by Fourier's Law:

$$Q_x = -kA_c \frac{dT}{dx} \quad (2)$$

Here, Q_x is the rate of heat transfer. k and A_c are the thermal conductivity and cross-sectional area of the colder surface respectively while dT/dx is the temperature gradient in the x direction. The negative sign indicates the direction of heat transfer leaving the hot surface into the cooler surface.

Convection is described by Newton's Law of Cooling which states that the rate of heat lost from a body is proportional to difference in temperature between the hot body and the surrounding fluid. In context, it is the rate of heat lost by the hot surface to the surrounding cooler fluid.

$$Q = hA_s \Delta T \quad (3)$$

Here, Q is the rate of heat transfer, h is the convective heat transfer coefficient of the cooler fluid, A_s is the surface area of the hot surface while ΔT is the temperature difference between them. The heat transfer coefficient is dependent on conditions in the boundary layer which is influenced by the hot surface geometry, the nature of the fluid motion and a variety of thermodynamic and transport properties of the fluid.

From equation (2), for a given size of the body, we can increase the rate of heat transfer due to conduction by using a material of higher thermal conductivity. From

equation (3), we can increase the rate of heat transfer due to convection either by increasing the h and/or reducing the temperature of the cooler fluid, thereby increasing ΔT and/or increasing the surface area (A_s) available for heat transfer. h can be increased by increasing the fluid velocity. However, only increasing the fluid velocity is either insufficient to obtain the desired heat transfer rate and often the costs associated in doing so involves increasing the pumping power requirements which is unfeasible (Incropera & Dewitt, 2011).

Thus, the feasible option left for enhancing heat-transfer is increasing the surface area by employing the use of extended surfaces. As shown in Figure 1-4, extended surfaces are projections from a surface that help increase the rate of heat transfer primarily by increasing the surface area available for convection.

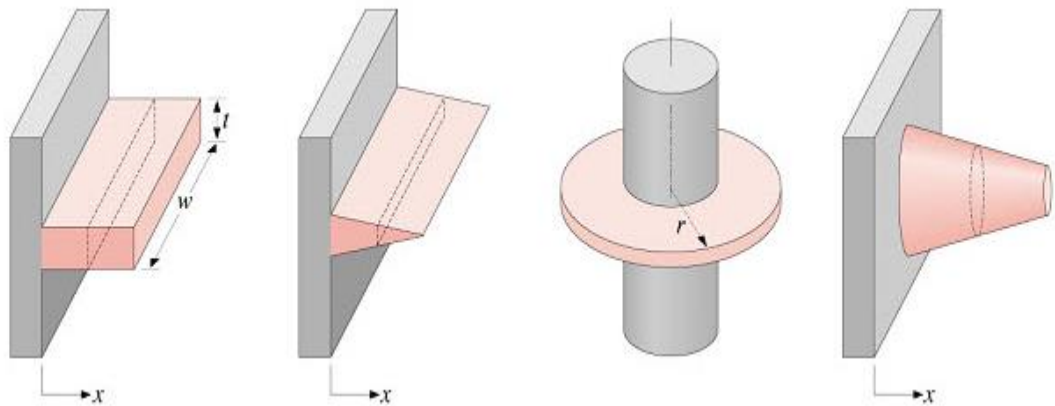


Figure 1-4. Variety of Extended surfaces (Incropera & Dewitt, 2011)

Figure 1-5 shows the benefits of using extended surfaces to enhance the heat transfer rate. As compared to a flat surface, extended surfaces help increase the surface area available for convection as shown in Figure 1-5(a). As seen in Figure 1-5(b), the extended surface is

in physical contact with the hot, flat surface.

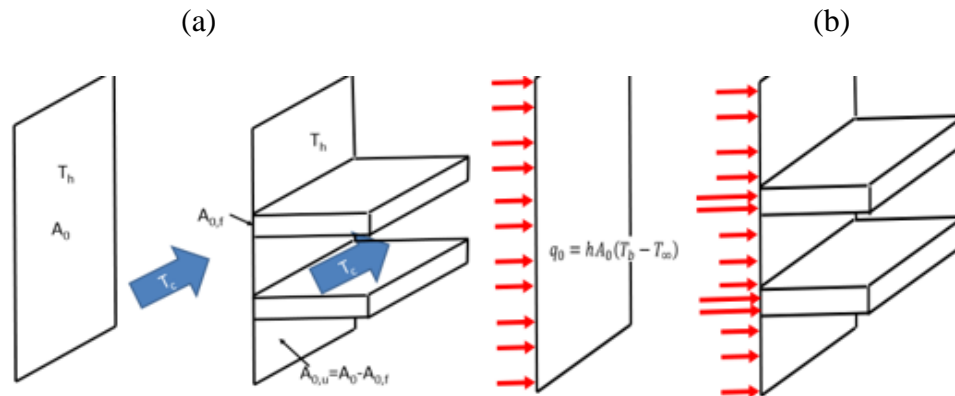


Figure 1-5. Comparison of benefits of using extended surfaces with a flat surface.

(a) net increase in surface area (b) increased heat flux through the surface

(Dr. Ricklick's lecture slides, 2015)

Extended surfaces are usually made from materials having high thermal conductivity and hence, heat transfer due to conduction is also increased. Extended surfaces find their applications in gas turbine cooling in the internal channels of the blade as pin-fins and ribs which are described in detail in the next section.

1.3 Turbine Blade Cooling Methods

Figure 1-6 shows the various cooling techniques used at the different sections of a gas turbine blade. Starting at the leading edge, film cooling is an external cooling method in which cool air bled from the compressor is ejected from holes on the hot surface of the blade as shown in Figure 1-6. Due to this ejection, the cool air forms a layer or film along the external surface of the blade. This layer of cold air helps reduce the thermal loads on the blade and helps in maintaining the blade surface temperature within permissible limits.

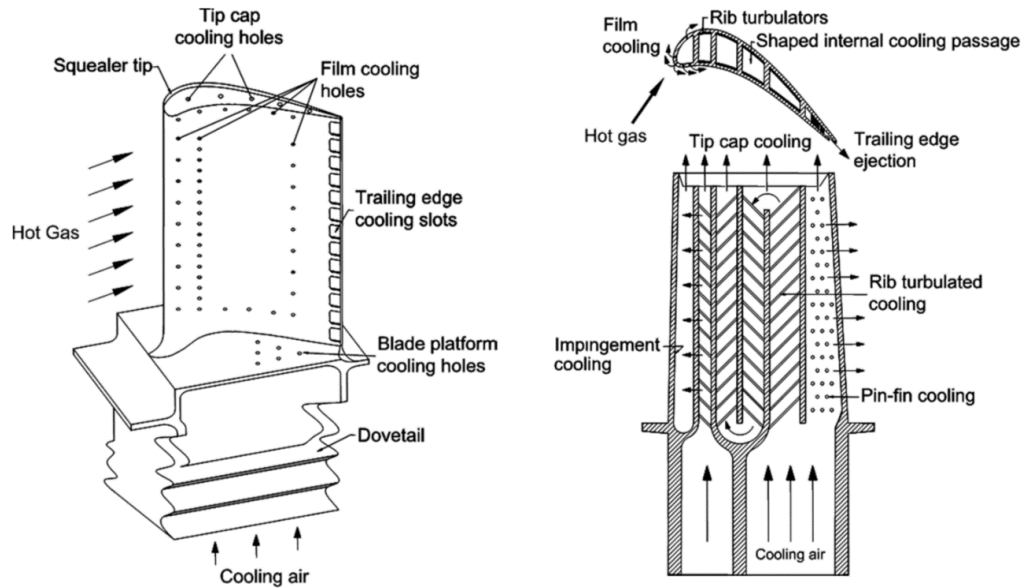


Figure 1-6. Blade cooling techniques (Han, 2004)

Impingement cooling is a type of internal cooling technique predominantly used near the leading tip edge of the gas turbine blade. As the name suggests, multiple jets of coolant ejected from internal holes impinge on the surface of the hot blade at the leading edge and help enhance the heat transfer.

Rib-turbulated cooling is the use of ribs, which are protrusions placed commonly on the two opposite walls of the internal channel of a gas turbine blade. These ribs act as flow obstructers and help enhance mixing in the section in which they are placed. The function of a rib is to trip the boundary layer of the incoming flow such that the flow separates and then re-attaches after the rib, creating re-circulation zones which augment the level of the turbulence in the channel and ultimately enhance heat transfer. Since it disturbs only the near wall flow, the pressure drop in the channel is within acceptable limits. (Han, 2004).

Pin-fin cooling is the use of a bank of extended surfaces at the short and narrow

trailing edge of the gas turbine blade. Like ribs, they help augment turbulence and mixing in the internal channel for heat transfer enhancement of the hot endwalls of gas turbine blade at the trailing edge. Figure 1-7 is an image of the in-house pin fin rig test section showcasing several circular cylindrical pins.

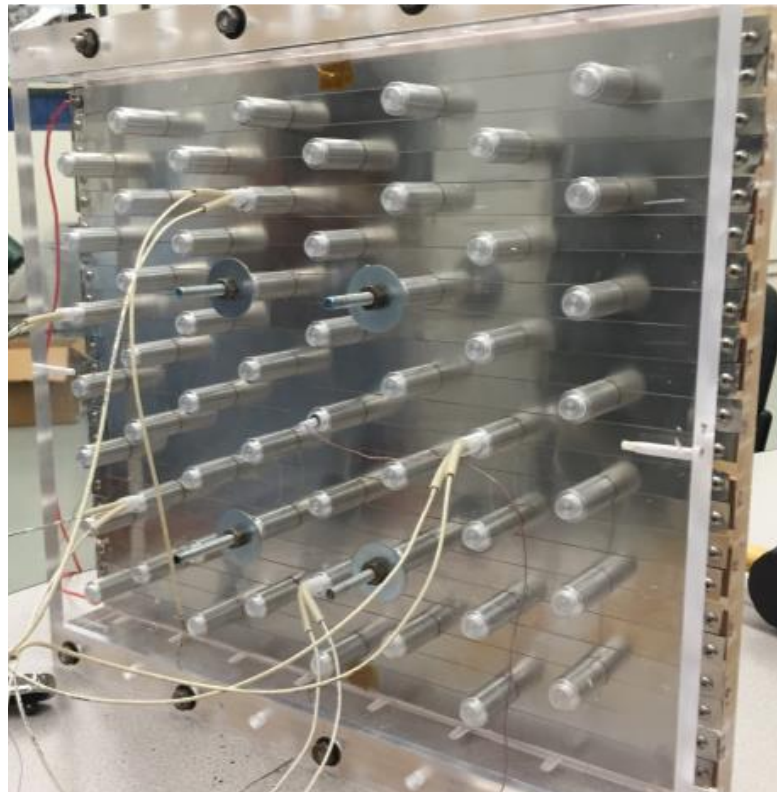


Figure 1-7. In-house pin-fin rig test section.

Pin-fins could be of several different shapes but the most commonly preferred for experimental investigation are circular cylindrical ones due to the ease of manufacturing. (Ames et al., (2006,2007), Chyu et al (1999), VanFossen (1981), Metzger & Haley (1982), Lawson et al., (2011)).

Figure 1-8 shows the two typical arrangements of arrays used in a pin-fin cooling channel. It also shows the typical nomenclature used for the non-dimensional distances between the pins in the streamwise (X/D) and spanwise (Y/D) direction. Distances are

usually normalized using the pin diameter (D). For an inline array, the rows are arranged in such a way that pins of consecutive rows are right behind each other. For a staggered array, the rows are alternatively arranged in such a manner that corresponding pins of any given row lie behind in the gap of the pins in the previous rows. Experimental investigations involving variation of parameters such as pin spacing, pin material, pin dimensions are discussed in detail in the literature review section.

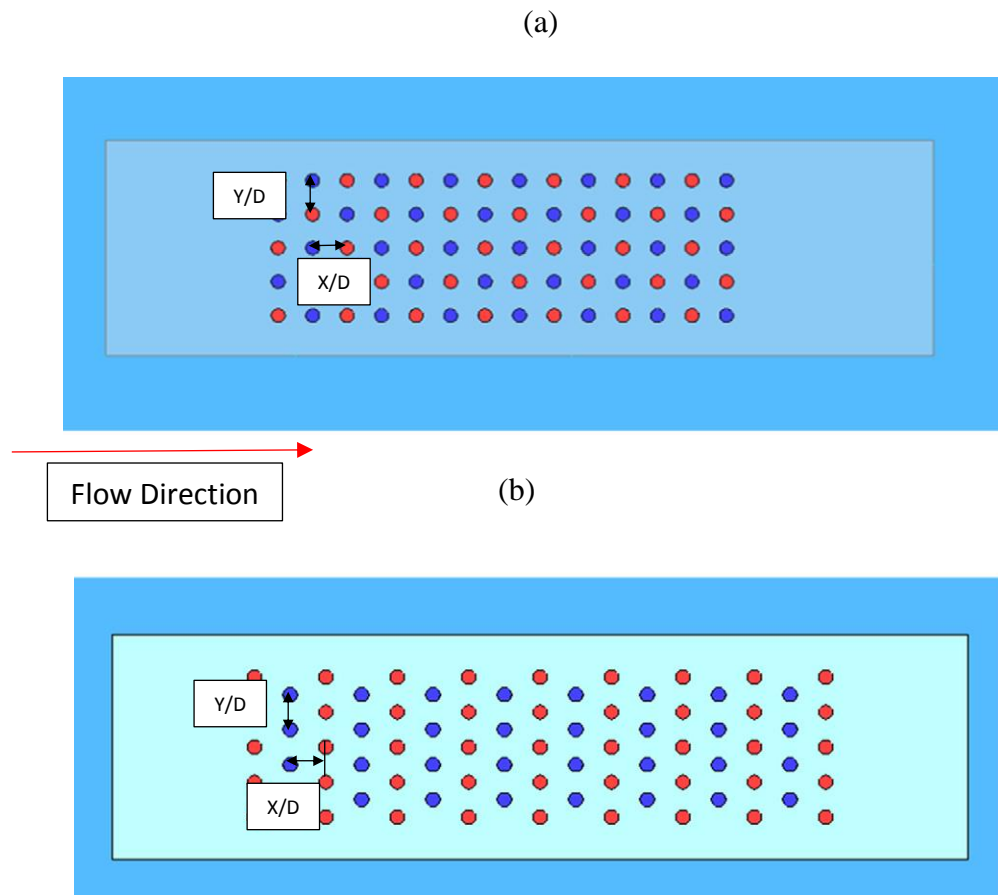


Figure 1-8. Types of array arrangement: (a) Inline array (b) Staggered array (Siw et al., 2012)

The use of pin-fin cooling at the trailing edge is 3-fold; to act as flow turbulators, to increase effective surface area and to provide structural support at the short and narrow

trailing edge. The primary objective of this study deals with the experimentation involving pin-fin channels and hence the next section describes some of the features of pin-fin channel in detail.

1.4 Pin-Fin Channel Flow Features

Some of the main characteristics of an internal cooling channel with a pin-fin array are regions of accelerated flows between the pins, stagnation flows, localized low and high pressure regions, flow separation zones and the presence of horse-shoe vortices at the endwall that contribute towards enhancing the rates of convective heat transfer (Ames (2006), Chyu (1999), Metzger (1982)). Figure 1-9 highlights some of the flow features at the end-wall caused due to flow obstruction by a single pin-fin.

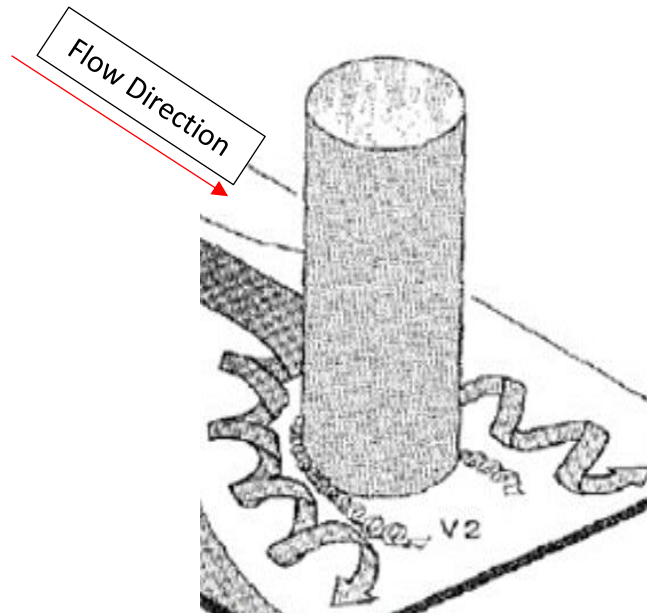


Figure 1-9. Flow features around a single cylinder. (Nguyen et al., 2012)

The presence of the pin causes the cooling air to stagnate on the cylinder surface

facing the flow, accelerate around the sides before separating due to the adverse pressure gradients (Celli, 1997). Figure 1-9 also shows the horse-shoe vortices formed at the endwall as the cooling air is forced to flow around the cylinder. Presence of horse-shoe vortices are not preferred from the aerodynamic point of view as they cause performance losses. However, in a pin-fin channel, these vortices break up the boundary layer on the end walls and produce high shear stress beneath it which results in high heat transfer from the end walls (Chyu et al., 1999).

Figure 1-10 is an image of a computational simulation of flow in a pin-fin channel. Clearly visible in this figure are the vortices created behind the pin due to flow separation at the sides. The resulting unsteady shedding of vortex caused by separation results in the chaotic mixing of cooling air on the back surface of the pin thereby driving heat transfer rates in this region (Ames & Dvorak, 2006).

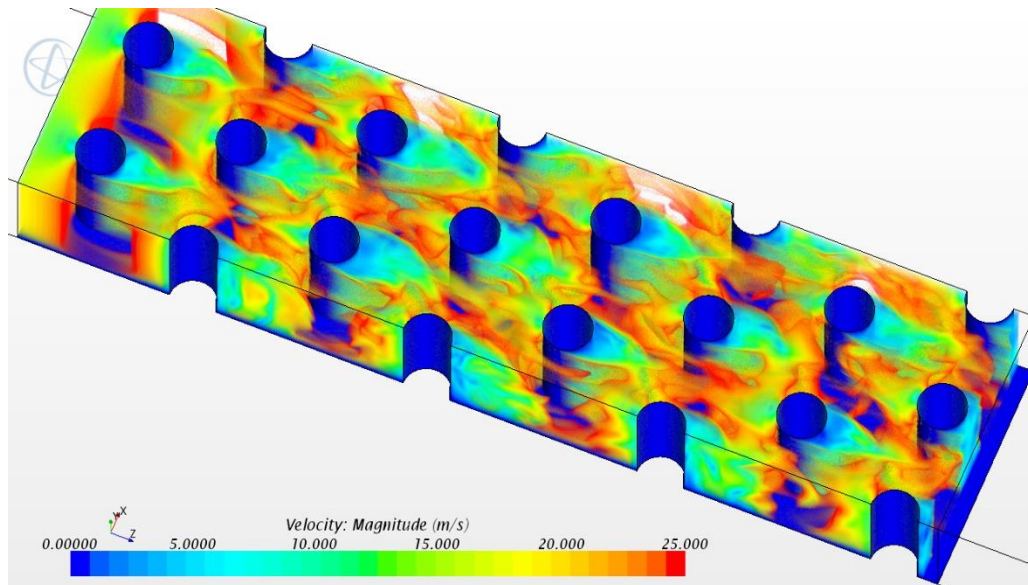


Figure 1-10. CFD simulation showcasing the flow features of a pin fin channel. (Fernandes, 2015)

1.5 Experimental Measurement Techniques

Thermocouples, naphthalene sublimation, thermo-chromic liquid crystals, IR cameras, temperature sensitive paint (TSP) are the different means of obtaining temperature data from an experimental setup. TSP, thermo-chromic liquid crystals, IR cameras are used to obtain high resolution, highly localized data of the entire test surface whereas thermocouples are attached at discrete points of interest.

The naphthalene sublimation technique involves dipping the test object in liquid naphthalene for one second, which after cooling forms very thin layer on the surface. After coating, the test objects are stored in a tightly sealed plastic box for at least 15 hours so that they attain thermal equilibrium with the surrounding air. Before the test run, each of the components are weighed using a highly sensitive and accurate electronic balance. After the heated test, the setup is individually weighed again and the difference in the weight yields the amount of naphthalene that sublimated during the run. Using a mass transfer analogy, the Nusselt number is obtained.

IR cameras measure the radiation emitted by the hot test surface. This radiation is a function of not only the temperature but also of the emissivity and reflectance of the body. The radiant energy is related to the temperature and the emissivity of an object as given by the modified Stefan-Boltzmann law. Although the relationship is linear, the emissivity of a body itself is dependent on the material, surface finish and viewing angle (Liu, 2007). If the emissivity of the body is less than unity, the body reflects some of the radiation from the surrounding objects as well leading to an error in temperature measurement. The IR system comprises of an IR radiation detector, an optical system to concentrate the radiation on the detector as well as a scanning mirror. The detector is usually cooled by liquid

nitrogen or Peltier cooler to minimize detector noise. Besides, the optical access window needs to be of Germanium material since standard silica glass, acrylic and quartz are opaque to infrared radiation (Liu, 2007).

Thermochromic liquid crystals are commonly used to qualitatively study heat transfer characteristics and only recently have been used to quantify heat transfer coefficients (Uzol & Camci, 2005). There are certain organic compounds that act neither like an isotropic liquid nor a non-isotropic crystalline solid but rather something in the middle of both these phases. These compounds are referred to as liquid crystals or mesophases. These liquid crystals react to changes in temperature, shear stress and electromagnetic fields by emitting light of corresponding wavelength. This is due to the molecules of these crystals stretch or contract depending on the change in temperature, shear stress and electromagnetic fields. Shear stress sensitivity can be made insignificant by encapsulating these crystals in a polymer while maintaining its temperature dependency. Although these liquid crystals can be handled easily, to capture the color change, the background of the test section must be painted completely black. One of the major disadvantages of using TLC is that the calibration curve is sensitive to the viewing angle and the lighting and hence can cause problems if used for quantitative applications (Liu, 2007).

Each of these temperature measurement techniques described here excluding TLC involves machining of the test section or making arrangements extraneous to the experimental setup. Also, the pin surface and endwall measurements need to be taken separately. Thus, there is a need for a non-intrusive prediction of surface average heat transfer coefficients which provide for faster turn-around times for the testing of different geometries by reducing setup time and cost albeit at additional post processing complexity.

2. Literature Review

A significant amount of studies have been conducted with regards to pin-fin cooling at the trailing edge of the turbine; experimentally as well as computationally. Some of the earliest works included trying to correlate the heat transfer characteristics between long tubes in cross flow heat exchangers and very short pins in plate-fin heat exchangers with pin-fin channels in a turbine blade. The difference between the three cases being in the height to diameter ratio (H/D). The pin-fins in an internal cooling channel of a gas turbine blade have a H/D ratio between the other two applications. Armstrong and Winstanley(1988) found that the interpolation between the two extreme cases did not accurately predict the performance characteristics of pin-fins in a gas turbine blade. The effect of conducting and non-conducting array of pins on surface average Nusselt number was studied by Metzger & Haley (1982, 1984) and by VanFossen (1982). Investigations were also done to obtain correlations for staggered and inline arrays by a host of researchers. (Sparrow (1980,2004), VanFossen (1982), Metzger et al., (1982), Chyu (1998)). Alternative pin geometries were compared against the baseline circular cylindrical pins for their pressure loss benefits by Goldstein et al., (1994), Chyu (1996, 1998) and Camci et al., (2005). Pin and row removal studies were also conducted to investigate the pressure loss and heat transfer characteristics by Sparrow & Molki (1982) and recently by Kirsch et al. (2014).

As the focus of research areas in regards to pin-fin cooling changed over the years, so did the experimental measurement techniques. In the 1980's, thermocouples were the preferred method of acquiring temperature data (Metzger & Haley (1982), VanFossen (1982, 1984) Sparrow (1980)). In the 1990's, heat transfer characteristics of the pin surface

were studied via a mass transfer analogy using a naphthalene sublimation technique (Goldstein et al., (1994), Chyu (1998,1999), Sparrow (1984). In the late 90's and 2000's, non-intrusive techniques such as IR and TLC were used to acquire endwall and pin surface data (Camci et al. (2005), Ames et al., (2007), Lawson et al. (2011), Kirsch et al., (2013)). Some of these studies are reviewed in detail in the following section.

VanFossen (1981, 1984) investigated the effects of pin height and pin inclination in a pin fin array. For his experiments, he utilized a staggered array of 4 rows but used two different set of pins. The first set of pins had an $H/D= 0.5$ and $X/D= 2$ while the configuration of the other set of pins was twice of this. Two separate arrays consisting of wooden and copper pin arrays were used to isolate and study the contribution of endwall and the pin surface individually. Only the endwalls were heated and maintained at a constant temperature. Thermocouples were used to obtain temperature data. He found that heat transfer coefficients on the pin surface were about 35% higher than the endwall. Inclined pins were found to have the same heat transfer characteristics as compared to the pins that are perpendicular to the endwall. Another study conducted by Brigham and VanFossen (1984) concluded that short pin fins indicated lower levels of heat transfer compared to longer pins of same design and that heat transfer augmentation is strongly dependent on the H/D ratio.

In order to compare the effect of conducting and non-conducting pins in a pin-fin channel experiment, Metzger & Haley (1982) used copper and balsa wood cylindrical pin-fins for their experimentation. The H/D of the pins were 1 and the pins were placed in a moderately dense manner ($\sim X/D=1.32-5$). Both endwalls were heated and had foil heater segments for each row, powered individually. The heat flux on each of these individual

segments were adjusted till an isothermal wall boundary condition was achieved that is the temperature difference between all segments was negligible ($\pm 0.1^\circ\text{C}$). Figure 2-1 is a plot of row average Nusselt number for conducting and non-conducting pins at different Reynold's numbers.

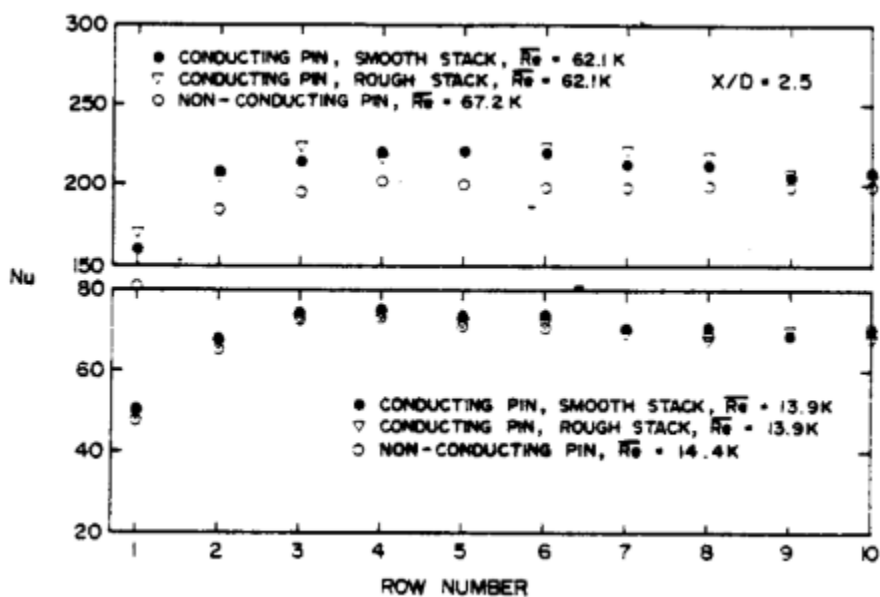


Figure 2-1. Row averaged Nu for conducting and non-conducting pin arrays. (Metzger & Haley, 1982)

Since this was a study to obtain row averaged Nusselt number, thermocouples were used at each row to obtain temperature data. Additional thermocouples were attached to account for failure. For each array configuration, pin type and flow rate, 2 power levels were used, corresponding to segment temperatures approximately 6°C and 12°C above the duct flow bulk temperature. Figure 2-1 shows that the difference in Nusselt number between conducting and non-conducting pins is negligible for the low Reynold's number case. Similar to many other researchers, they observed heat transfer augmentation up to row 3 and then a periodically fully-developed rate of augmentation till the last row.

Chyu et al., (1990, 1999) used a naphthalene sublimation technique to study the individual heat transfer contributions from the pin as well as endwall using a mass transfer analogy. This setup helped them to ensure that the entire wetted surface in a pin fin channel was thermally active. He also noted that the variety of thermal boundary modelling used by researchers for a pin-fin array did not influence the general trends of heat transfer as significantly as the individual magnitudes due to bulk flow temperature variations.

The mass transfer co-efficient or the Sherwood number is analogous to the Nusselt number in heat transfer. Chyu (1999) used aluminum pins and investigated both inline and staggered arrays for Reynold's numbers of 7650, 16800 & 23100. A constant wall temperature boundary condition was utilized at the endwall. Figure 2-2 shows the row averaged Sherwood numbers at the pin surface and endwall for different Reynold's numbers. As we can see from Fig. 2-2, he concluded that the heat transfer coefficient on the pin surface is higher than that on the uncovered end wall by approximately 10-20% as compared to 30-40% obtained by VanFossen(1982)

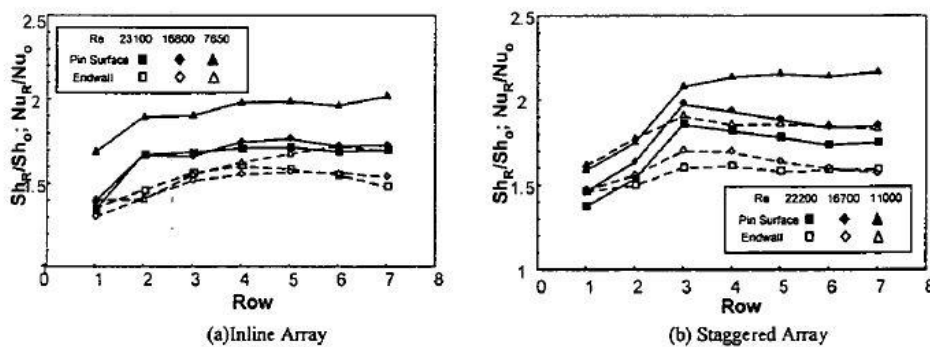


Figure 2-2. Row averaged Sherwood numbers at pin surface & endwall for different Reynold's numbers. (Chyu, 1999)

Since the endwall represents about 80% of the wetted area, he believed that an experimental approach focused solely on the endwall contribution is more representative of the channel than the one focused solely on pins which the author believes grossly

undermines the influence of the pins on endwall heat transfer.

Uzol and Camci (2005) conducted a study to compare endwall heat transfer enhancements and total pressure loss between circular, elliptical and a pin based on NACA 0024 airfoil. They had an $H/D=1.5$, $S/D=X/D=2$ for a staggered array of 2 rows of pins. Their test section containing the pin-fin array and the heated section was placed 4 & 2 pin diameters distance from the entrance respectively. They used a constant heat flux boundary condition on the endwall, the pin was not heated. Endwall heat transfer data was obtained by using liquid crystal thermography. A detailed description of liquid crystal thermography can be found here (Wilberg et al., 2004). It was observed that the circular fin array had 27% higher Nusselt number as compared to the elliptical and the NACA shaped pins. However, the total pressure loss in the circular channel was found to be 46.5% higher than the elliptical fin and 59.5% higher than the NACA shaped pin. They also used a parameter referred to as the specific friction loss in an internal channel which is the ratio of average friction factor to the average Nusselt number for the channel to compare overall performance of the pin shapes. The elliptical and the NACA fin had a lower specific friction loss as compared to the circular ones due to the pressure loss benefits on the account of delayed flow separation.

Ames et al., (2006) studied the flow physics that is characteristic of a pin fin channel by measuring turbulence intensity and acquiring pin-fin midline heat transfer and pressure distribution around the pin for Reynolds numbers of 3000, 10,000 and 30,000 as shown in Figure 2-3. Their Reynold's number was based on the maximum velocity between the pins and the pin diameter. They had a $H/D=2$, $X/D=S/D= 2.5$ which is comparable to the in-house rig which is the primary reason for comparing the veracity of the results obtained

from this study to the work done by Ames et al. Hot-wire anemometry was used to measure the fluid characteristics. They used a constant heat flux boundary condition on the pin surface and had a heated entrance length to ensure that the flow is thermally developed when it reaches the test section. Data was acquired from a single heated pin by placing it in different rows, using 24 equally spaced thermocouples placed around the pin. They found that heat transfer is the highest in the 3rd row due to highest effective velocity while heat transfer augmentation due to turbulence is the highest in row 4.

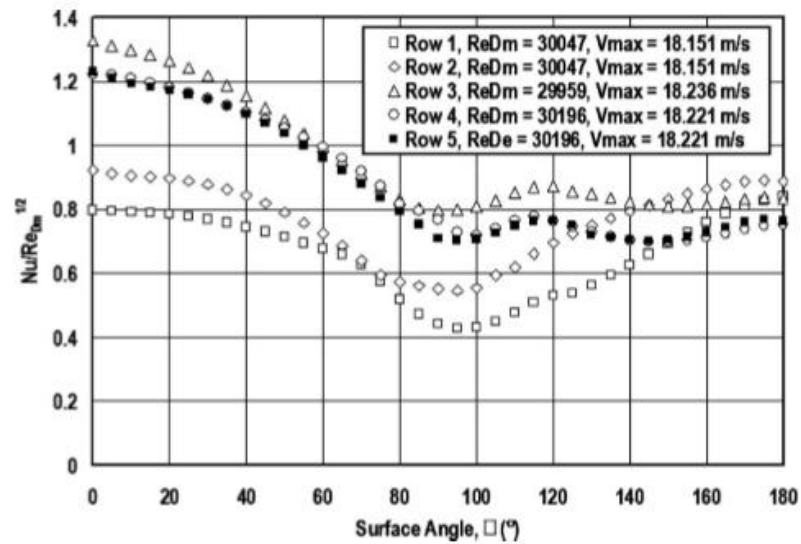


Figure 2-3. Midline $Nu/Re^{0.5}$ distribution of different rows for $Re=30,000$
(Ames, 2006)

Lawson et al., (2011) investigated the effect of spanwise and stream-wise spacing on heat transfer augmentation and pressure loss in a low aspect ratio pin-fin channel and Reynolds number ranging from 5000 to 30,000. Nusselt number contours of the endwall were acquired by measuring temperature with an infrared (IR) camera through a Zinc Selenide window which allowed for IR transmittance. A constant heat flux boundary condition was maintained since both the endwalls were heated with the help of Inconel

strips connected in a serpentine pattern. Figure 2-4 shows the endwall Nusselt number contour for varying streamwise distances.

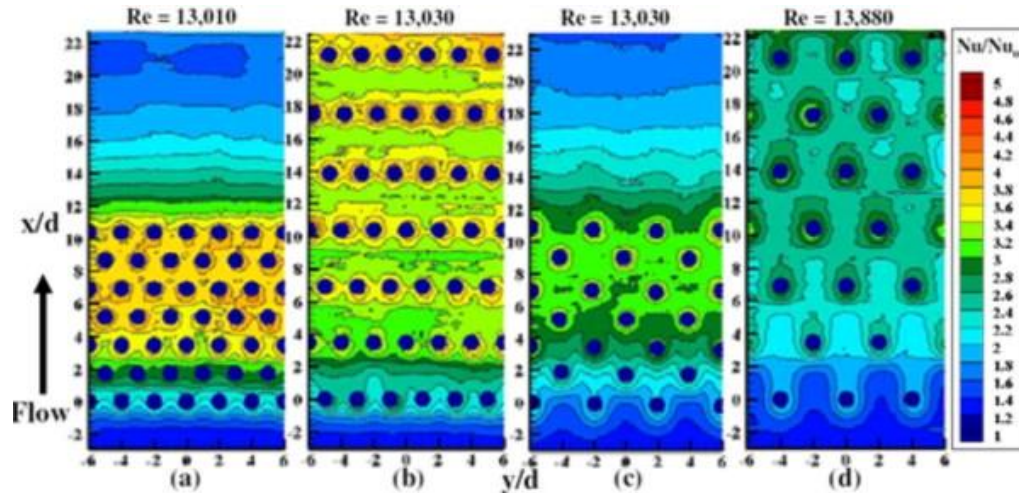


Figure 2-4. Endwall Nusselt number contour for $Re=13,000$ for different streamwise spacings. (Lawson et al., 2011)

They found that with increase in Re , heat transfer augmentation at the pin surface per row decreases. The reason being that at low Re , turbulence created by the pins is much greater. End-wall heat transfer is affected more by stream-wise spacing than by spanwise spacing. Also, pressure loss in the channel is more dependent on spanwise spacing owing to flow blockage.

At the same facility, Kirsch et al. (2013) investigated the heat transfer characteristics for circular and oblong shaped pin arrays at Reynolds Number ranging from 10,000 to 30,000, for $H/D=1$ and $S/D=2, 2.5$ and 3. Figure 2-5 shows a plot that compares circumferential Nusselt number distribution between oblong and cylindrical pin-fins. Since the oblong pins are inherently longer in the stream-wise direction, they found that the laminar boundary layer that forms along the oblong pin is able to transition to turbulence.

As a result, the heat transfer decreases until the point at which the transition to turbulence occurs. A sharp increase in heat transfer can be seen at this point, which is very evident from the secondary peak in the Nusselt number that can be seen in the above figure.

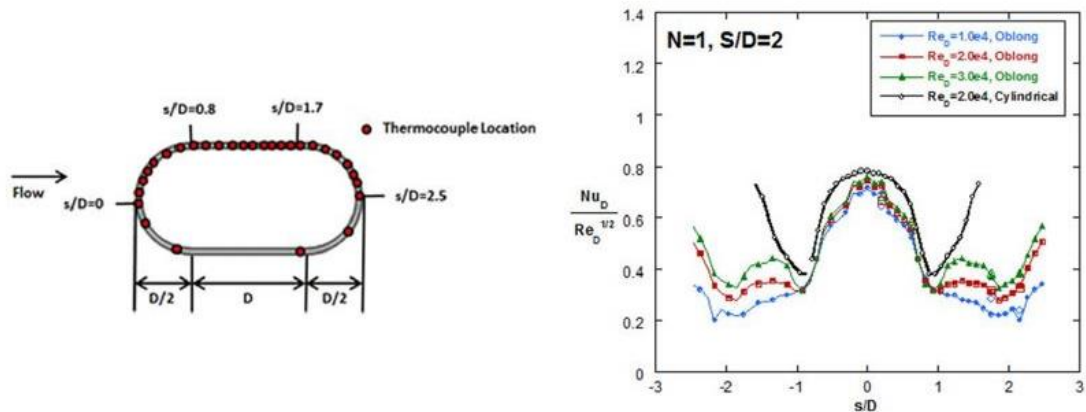


Figure 2-5. Circumferential Frossling number distribution for different Re for cylindrical and oblong pins. (Kirsch et al., 2013)

Since the primary focus of this study is an experimental investigation, only a couple of computational studies have been reviewed and discussed ahead. A computational study comparing the heat transfer enhancement and pressure loss of different cross-sectional shapes of pins was conducted by Sahiti et al (2006). Figure 2-shows the cross-sections of the various shapes that were tested.

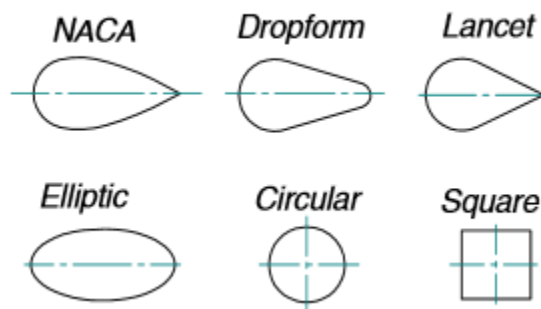


Figure 2-6. Cross section of pins tested. (Sahiti et al., 2006)

The boundary conditions imposed on the computational domain were very similar to the in-house rig at PTML i.e staggered pin-fin array with only the bottom endwall heated. However, this study was done for very low Reynold's numbers ranging from 200-750 and application in a pin-fin micro channels for electronic components.

They found that the flow in a staggered pin fin array is characterized by one impact point from which the boundary layer develops symmetrically around the pin surface. It was observed that flow separation occurs earlier for the circular and lancet shapes which results in greater total pressure loss when compared to the other shapes. Array averaged Nusselt number was also obtained as a function of Reynold's number for the different shapes as shown in Figure 2-7.

Pressure drop across the channel was non-dimensionalized as the Euler number and given as function of Reynold's number for the different shapes in Figure 2-8. It can be clearly seen that the highest pressure drop was observed for the square shaped pin, followed by the circular-cylindrical shape, which is the most common shape of pin-fins investigated due to the sharp gradients in cross-sectional shape.

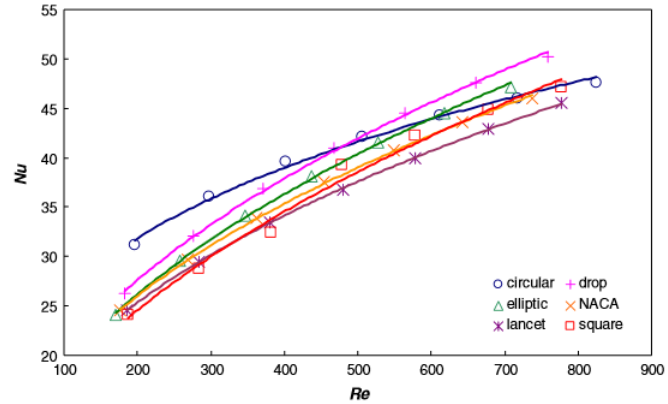


Figure 2-7. Array averaged Nu as a function of Re for different shapes.

(Sahiti et al., 2006)

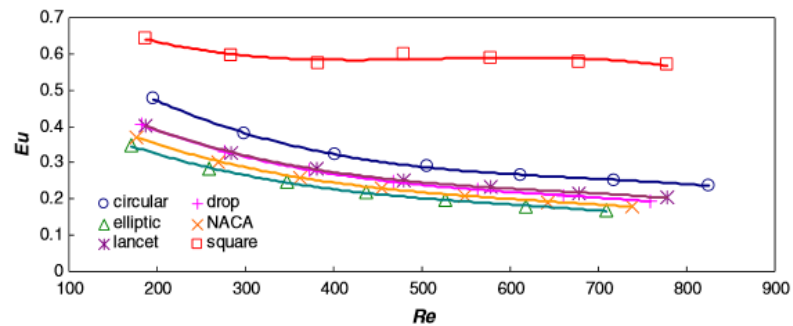


Figure 2-8. Array averaged Eu as a function of Re for different shapes.

(Sahiti et al., 2006)

More recently, alternative pin geometries that are inspired by nature were also investigated numerically by the author (Pai et al., 2017).

These designs were inspired by the shape of the harbor seal whisker as shown in Figure 2-9. (NASA, 2014). The undulated shape of the whiskers results in reduced vortex excitation and smaller, organized flow structures behind the whisker. (Hanke et al., 2010). In its application to turbine blades, reduced aerodynamic loading and total pressure losses have been observed (Shyam et al., 2015)

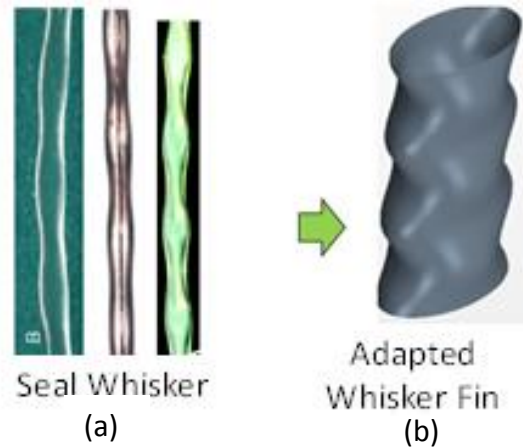


Figure 2-9. (a) Seal whisker (Hanke et al., 2010) and (b) Proposed bio-inspired cylinder. (Pai et al., 2015).

Figure 2-10 shows the various alternate geometries considered for this study.

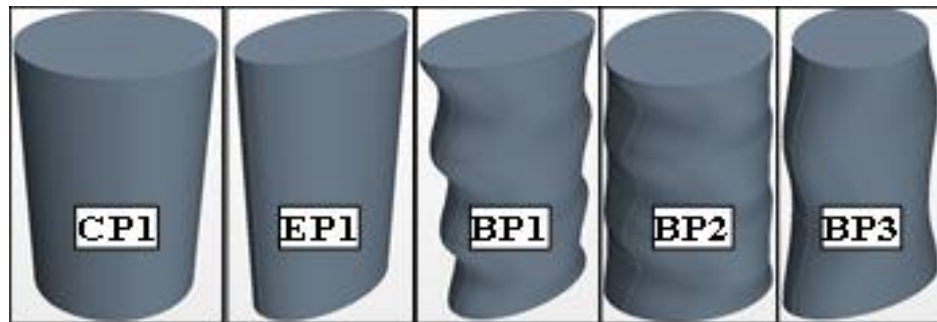


Figure 2-10. Alternate geometries considered for the study. (Pai et al., 2017)

The bio-cylinders analyzed in this study were adapted from models described in the literature. The heat transfer and pressure loss characteristics were compared to baseline circular and elliptical models for two Reynold's numbers. The BP2 geometry performed better as compared to the circular baseline and other models in terms of heat transfer enhancement by about 5% while EP1, the baseline elliptical model performed the best in terms of thermal performance at constant pumping power. It should be noted that all the alternative geometries (EP1, BP1, BP2, BP3) showcased significantly less pressure loss as compared to the circular baseline case (CP1).

3. Problem Statement

As we saw in the previous section, researchers have been using different thermal boundary conditions when studying the thermal performance of pin-fin arrays. Since the flow in an internal cooling channel of a gas turbine blade is turbulent, the heat transfer characteristics are highly dependent on the fluid properties i.e. Reynold's number and Prandtl number and show very weak dependency on the thermal boundary condition (Bejan, 2003). Each boundary condition arrangement has corresponding advantages as well as ensuing complexity in the experimental setup. The reason for using different thermal boundary conditions is to simplify the complicated experimental setup and as well as to compensate for manufacturing limitations. In most of the experiments, either the pin is heated or the endwall.

Since the flow-field in a pin-fin cooling channel is highly complex and non-uniform, many thermocouples would need to be attached to obtain data from the entire test surface. The use of thermocouples is accompanied by additional machining of holes on the pin and endwalls. Often, additional thermocouples are attached in the event of failure of the original thermocouple. Thus, for a pin-fin array, use of thermocouples is accompanied by large setting up times due to the additional machining that is required. Internal heat generation within the pin is required to maintain a sufficient temperature difference between the pin surface and coolant, reducing experimental uncertainty.

Thus, certain simplifications can be made either on the experimental side or the post-processing side for the ease and shorter turn-around times of testing. Validation tests need to be done with well-established experiments. In terms of the design process, experimental verification is the step following the elimination of the initial geometries

through numerical simulations. As we can see, there is a need for predicting average heat transfer coefficients on the surface of a fin through non-intrusive techniques to reduce the turnaround times associated with experimental setup.

The hypothesis of this study is that the base temperature of the pin can be used to obtain accurate pin surface average heat transfer coefficients. The new method prescribed in this thesis aims to simplify the setting up process at the cost of additional post-processing complexity.

The 3 major objectives of this thesis are listed below:

1) Obtain analytical solution and validate with existing solution.

First, an analytical solution is obtained for the unique boundary conditions of the in-house experimental setup. This solution is then validated by comparing it with an existing solution for an infinite fin with internal heat generation Bejan (2003).

2) Verify numerically using CFD

The analytical solution is then verified numerically in STAR-CCM+ first by using a prescribed pin surface heat transfer coefficient and for a second case of conjugate heat transfer, both for a single pin in an internal channel.

3) Verify experimentally and compare with Ames' paper (2006)

After the analytical solution is verified analytically and numerically, the in-house experimental setup is used to further establish confidence in the method by comparing generated results to the results given by Ames (2006). This paper was chosen to compare our results due to the similarity between experimental setups.

4. Methodology

4.1 Experimental Setup

The test section, shown in Figure 4-1, is manufactured from 2.54cm (1") thick optically clear acrylic. Figure 4-1 also shows the sCMOS camera used for recording TSP emission, the TSP excitation LED lights along with the current source. The working of TSP is detailed in the next section. Acrylic was chosen as it allows suitable optical access for TSP measurements, as well as its insulation properties. The current pin-fin array consists of 8 rows, having 7 full cylindrical, aluminum pins in each row arranged in a staggered manner. The arrangement for this study was also used for previous investigations by Fernandes (2015) and Prasad (2016).

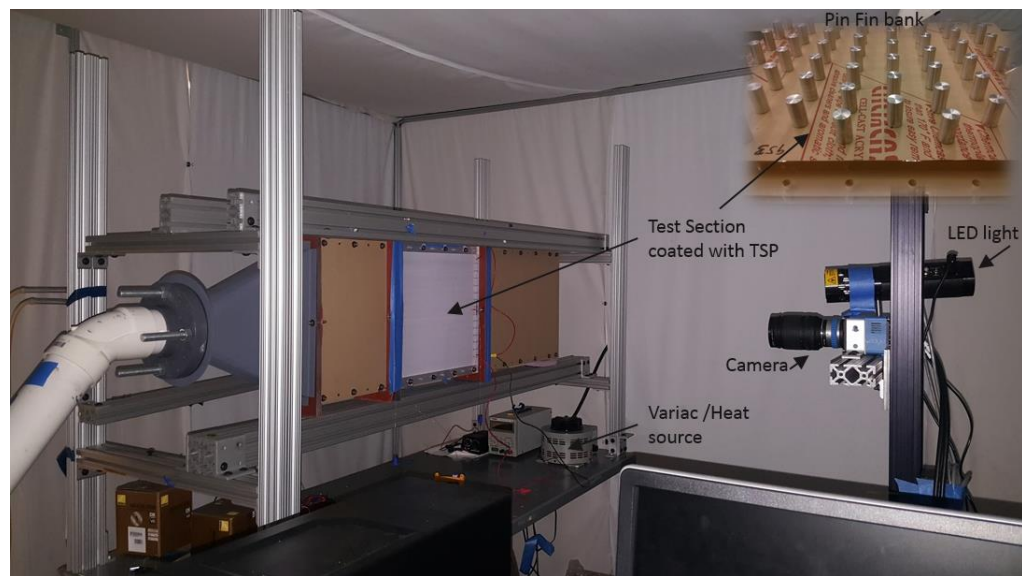


Figure 4-1. Experimental Setup.

Figure 4-2 shows the schematic of the flow loop used for the experiments. The centrifugal blower was operated in suction mode for all experiments. The flow was controlled using gate valves. The venture flow meter gave the difference in pressure

between the flow upstream and downstream which was used to determine the mass flow rate and ultimately the average velocity of flow in the channel.

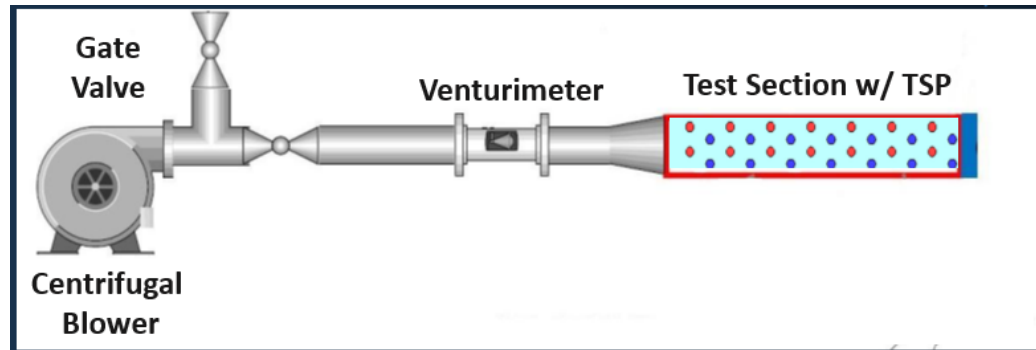


Figure 4-2. Schematic of Flow-loop

Figure 4-3 shows the non-dimensional distances in the channel. Taking the pin diameter as the reference diameter, the non-dimensional streamwise (X/D) and spanwise distance (Y/D) between the pins was chosen to be 3 based on previous research (Ames et al., (2006), Metzger & Haley (1982), VanFossen (1982)).

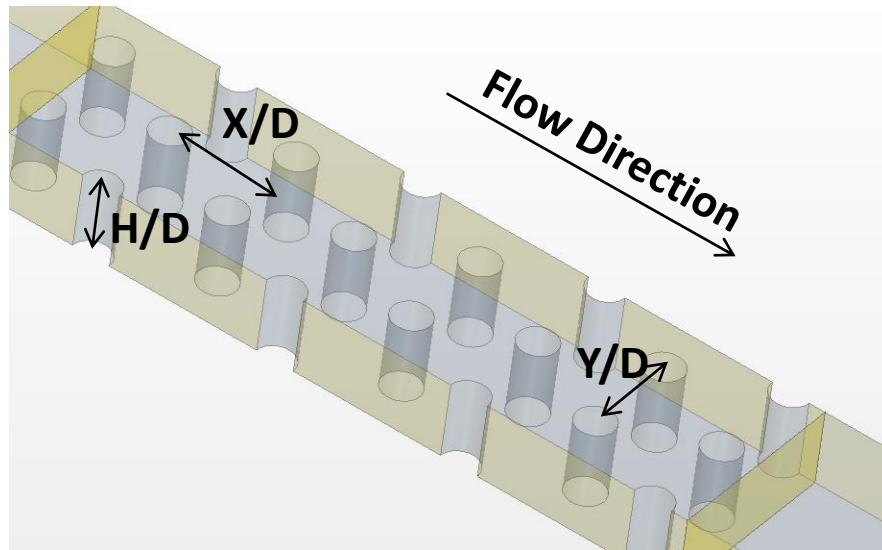


Figure 4-3. Non-dimensional distances.

The H/D distance of the channel for the study was maintained at 2. An entrance section of 10 channel hydraulic diameters in length was placed upstream of the test-section,

and an exit section of 5 channel hydraulic diameters was placed downstream. From the exit section, a transition duct was used to adapt the rectangular duct to circular PVC piping. This PVC piping connected the tunnel to a centrifugal blower was in operation under suction mode as seen in Figure 4-1 and Figure 4-2. Adiabatic inlet and outlet sections of 10 and 5 hydraulic diameters respectively, are attached just upstream and downstream of the test section.

Figure 4-4 shows a cross sectional view of the layout in the test section with a single pin. The thickness of the strips under the pin are exaggerated here for clarity. The pin is held between the two acrylic endwalls and the pin tip is flush fit into a cavity machined on the top endwall. The pins can be made of conducting (thermally active) or non-conducting material. For this study, they were manufactured from aluminum. The size of the pin was such that the Biot number was less than 1 and hence temperature distribution within the pin was uniform. The inner side of the heated wall of the test section was painted with TSP. Inconel strips were attached in series in a serpentine manner with the help of copper bus bars at the ends using a high temperature adhesive tape to provide a constant heat flux boundary at the wall as shown in Figure 4-4 for an investigation of a rib channel at the same facility (Prasad, 2016). The width of the Inconel strips was equal to the diameter of the pin placed on it (0.015m).

Kapton tape was used to prevent electrical contact wherever the pins were in contact with the Inconel strips on the bottom endwall. The Kapton and adhesive tape are 0.03mm and 0.02mm thick respectively, yielding a negligible temperature drop under normal operating conditions (estimated to be $< 0.1^{\circ}\text{C}$ for a typical high heat flux case).

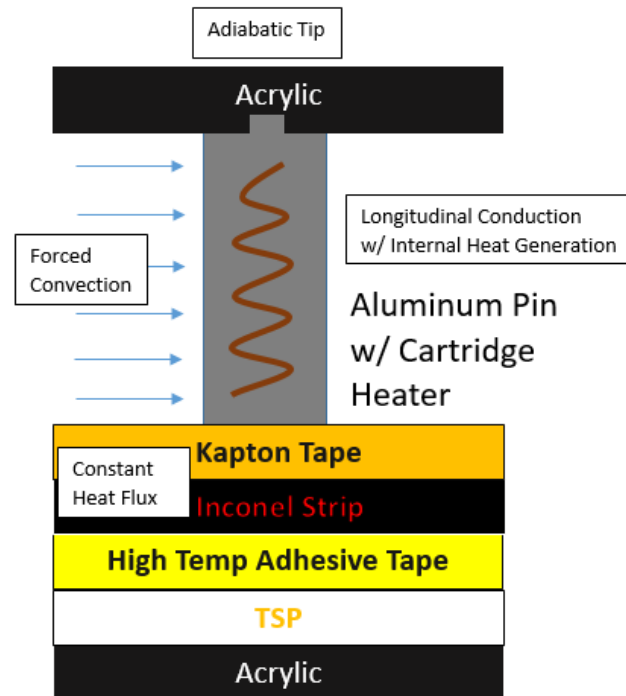


Figure 4-4. Layout of the test section with boundary conditions.

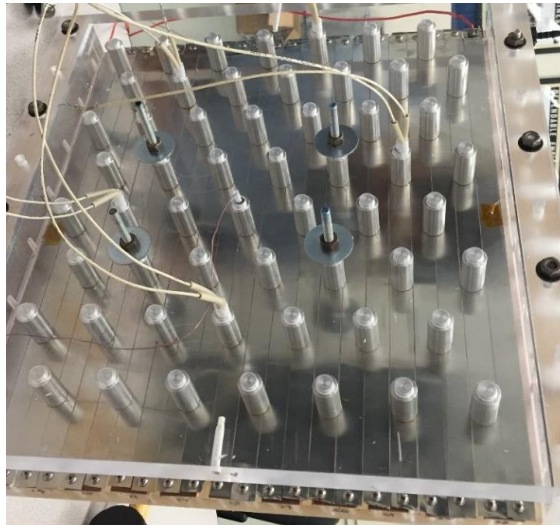


Figure 4-5. Serpentine arrangement of Inconel strips in the test section.

Omega high density cartridge heaters of 45W power, 2.54cm in length and 0.67cm diameter, were placed within cavities drilled inside single pins of rows 2,4 & 5 for comparison with Ames (2006) data for the same. A tight fit and thermal contact between the pin and the cartridge heaters was ensured by using thermal glue of high thermal

conductivity ($\sim 2.24 \text{ W/m-k}$). Individual cartridge heaters were connected in parallel and the cartridge heater circuit was then connected in parallel to the serpentine arrangement of Inconel strips, as shown in Figure 4-5. Individual shunt resistors of low and known resistance ($\sim 0.003 \text{ ohms}$) were connected in series with each arm of this setup. Potential drop across each arm was measured across the shunt resistor. The circuit diagram of the entire setup can be seen in Figure 4-6.

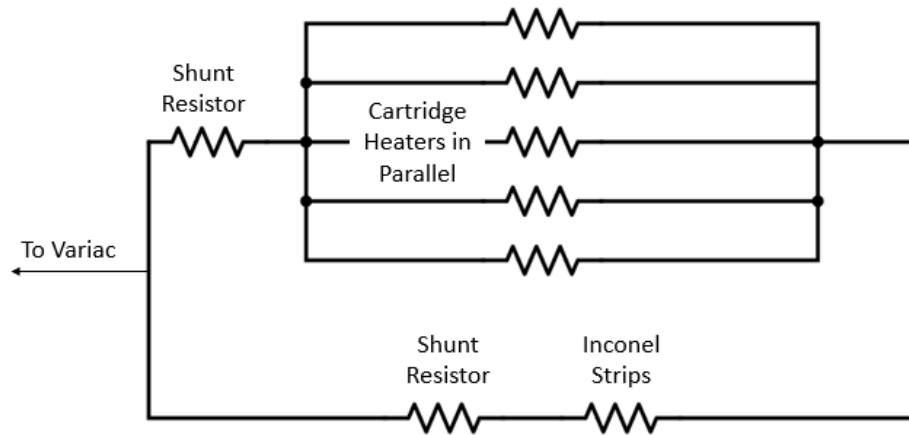


Figure 4-6. Circuit Diagram of the entire setup.

The heat flux supplied to this entire setup was controlled by varying the applied voltage using a variable AC transformer (Variac).

Thus, the thermal boundary conditions for the experimental setup are constant heat flux on the bottom endwall, internal heat generation in the pin via cartridge heaters, adiabatic tip at top endwall. Due to the high thermal conductivity of the pin, the heated pins can be assumed to be isothermal.

4.2 Temperature Sensitive Paint

TSP is a technique that can be used to obtain temperature data of the entire test surface. Another advantage is that it is a non-obtrusive technique and setting it up in terms of effort is relatively low as compared to the machining involved with the use of thermocouples. TSP is a luminescent paint containing fluorescent molecules suspended within a binder (Sullivan et al., 1995). When exposed to a light of adequate wavelength, these fluorescent molecules become excited and jump to a higher level of energy state. For this study, ISSI's UniCoat TSP was used (Innovative Scientific Solutions, Temperature Sensitive Paint) As obtained from the manufacturer, the excitation wavelength required for this paint was 380-520 nm and its emission wavelength was 500-720 nm. One of the methods by which these molecules return to their ground energy state is by emitting photons of a particular wavelength also known as luminescence. The alternative path to ground state is by thermal quenching, without emitting photons, the likelihood of which increases with increasing temperature. Thus, the emitted intensity is inversely proportional to the local temperature. This emitted light is of a longer wavelength and a scientific grade camera with a proper filter can be used to distinguish between the excitation light and the emitted light. Figure 4-7 shows the Jablonski diagram which shows the different energy levels of a molecule as well as the process by which a molecule can jump levels. There are two approaches in using TSP, a lifetime approach and an intensity ratio approach. The latter is used for this study. A detailed description of TSP methods is given by Liu (2006) and Sullivan (1995). The intensity ratio calibration involves plotting the intensity ratio against the percentage difference in temperature between the reference and data image as shown in Figure 4-8. Higher the temperature, lower is the intensity of light emitted because

then the molecules return to their ground state pre-dominantly by vibration (Liu, 2007).

Thus, the emission intensity decreases with temperature because of thermal quenching.

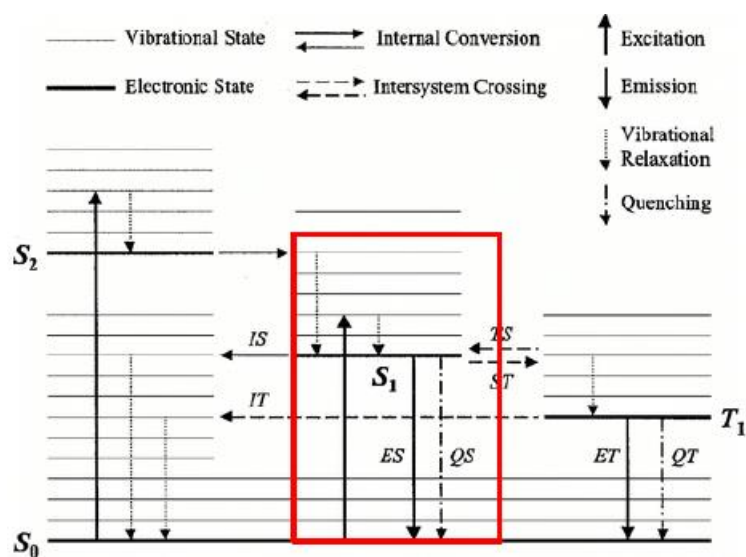


Figure 4-7. Jablonski Diagram (Bell, 2001)

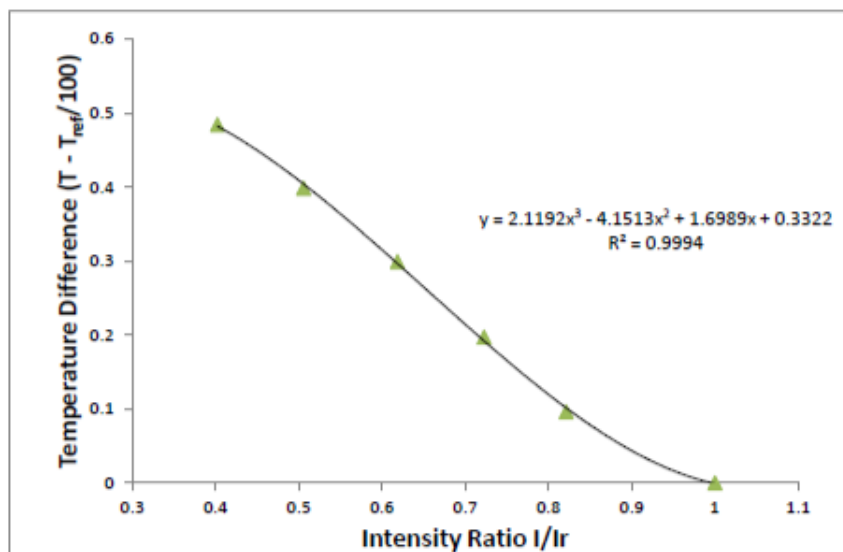


Figure 4-8. Typical TSP calibration curve (Fernandes, 2015)

First, a cold image is taken at a known reference temperature (i.e. room

temperature) and then the data image is taken after steady state (b) been attained by the heated setup. Figure 4-9 (a) is a representative raw reference image of higher intensity and known temperature while figure 4-9 (b) is a representative raw data image of lower intensity and unknown temperature prior to data reduction.

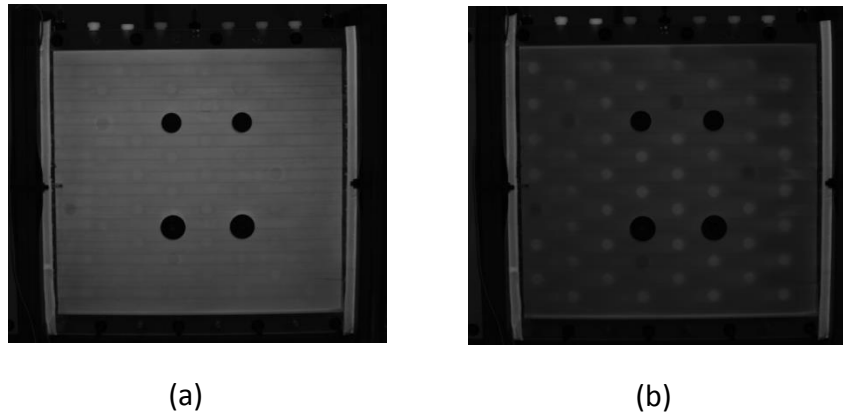


Figure 4-9. (a) Reference image of higher intensity, known temperature.

(b) Data image of lower intensity, unknown temperature.

Thus, by knowing intensity of both the images, the temperature of the reference image and the calibration curve, we can obtain the temperature of the hot image. The effective temperature range of TSP is from 0°C to 100°C. Both, TSP and thermocouples have a measurement uncertainty of $\pm 1^\circ\text{C}$ (Liu, 2007).

4.2 Data Reduction

Heat transfer that occurs due to convection is quantified and non-dimensionalised as the Nusselt number which is given by the following relation:

$$Nu = \frac{hD}{k} \quad (4)$$

Here, k is the thermal conductivity of air and D is the characteristic length, the pin diameter in the current study.

The heat transfer coefficient is defined from Newton's law of cooling as:

$$h = \frac{q''_{eff}}{(T_s - T_b)} \quad (5)$$

Here, q''_{eff} is the difference between the heat flux supplied to the system and the heat lost to the surroundings. Since acrylic is not a perfect insulator, some of the heat supplied to the Inconel strips in the test section leaks out to the surroundings. The amount of heat lost to the surrounding can be quantified using a heat leakage test, the results of which are discussed in further sections. The surface temperature of the endwall is measured using the TSP while the bulk temperature is based on the test section inlet and outlet temperatures measured using thermocouples. Thus,

$$q''_{effective} = q''_{supplied} - q''_{lost} \quad (6)$$

$$q''_{supplied} = \frac{I^2 R}{A_s} \quad (7)$$

Here, I is the current supplied to the Inconel strips, R is the total resistance of the Inconel strips and A_s is the surface area of the Inconel strips. The current supplied is measured using the voltage across a shunt resistor and by using Ohm's law. The resistance of the Inconel strips is calculated as:

$$R = \rho \frac{L}{A_c} \quad (8)$$

Here, L is the total length of the Inconel strips which are laid out in a serpentine manner in the test section and A_c is the cross-sectional area of the strips.

The bulk temperature is calculated as,

$$T_b^{i(x)} = T_b^{i-1(x)} + \frac{q(x)}{\dot{m}C_p} \quad (9)$$

The LHS is the bulk temperature of the current pixel in the x direction (streamwise) calculated using the bulk temperature of the previous pixel. $q(x)$ is the heat supplied per

pixel, \dot{m} is the mass flow rate into the channel while C_p is the specific heat capacity of the air based on the mean bulk temperature.

Mass flow rate through the channel was obtained by a venturi flow-meter of diameter $\sim 3''$. This was calculated using a calibration curve supplied by the manufacturer as shown in Figure 4-10. The accuracy as stated by the manufacturer was $\pm 1\%$ (Preso Venturi SSM user manual). The mass flow rate through the pipe was dependent on the difference in pressure, the density and temperature of the inlet air.

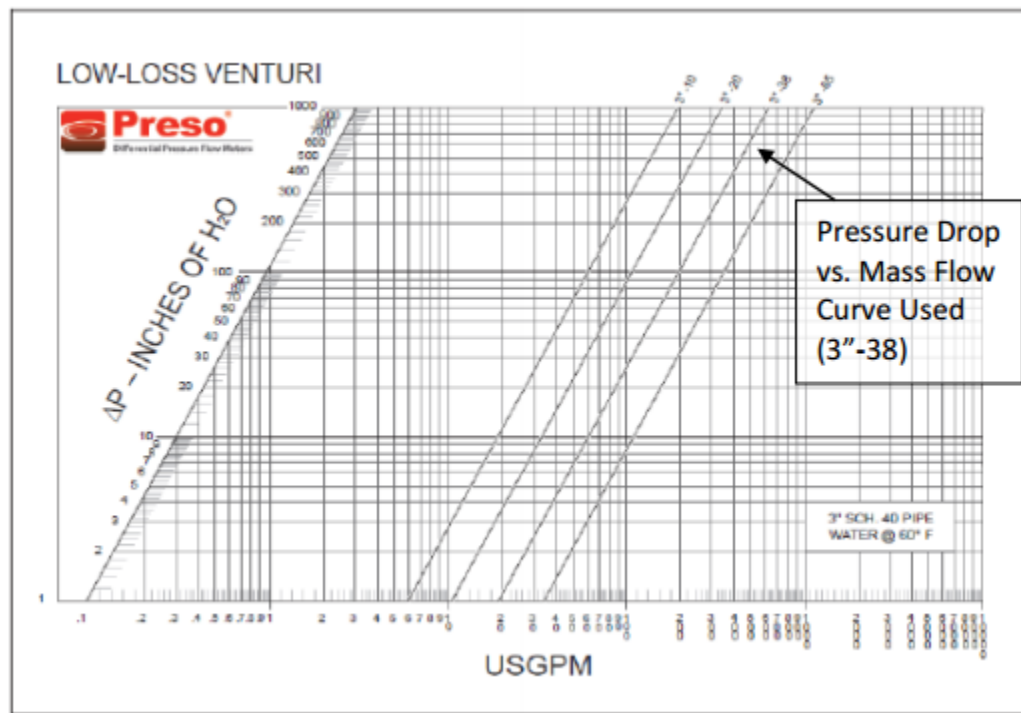


Figure 4-10. Pressure drop versus mass flow rate for the venturi-flowmeter.

Using the mass flow rate obtained, the Reynolds number through the channel is given by,

$$Re = \frac{\dot{m}D}{\mu A_{eff}} \quad (10)$$

D here is the pin diameter while A_{eff} is the effective cross-sectional area between the pins. The effective cross-sectional area is the same one used by Ames (2006) that is the

difference between the open channel area and the frontal area of a single row of pins.

As mentioned earlier, measurement uncertainty of a thermocouple and TSP is $\pm 1^\circ\text{C}$. From equation (5), for a constant wall heat flux and a temperature difference of 20°C , error in h is already around 10%. Previous investigations (Prasad, 2016) have also shown the reduced uncertainty in Nusselt number for a higher temperature difference. Thus, we need to ensure that the surface temperature is higher than the bulk flow temperature by at least 20°C to reduce our experimental uncertainty in determination of h . After repeated tests, it has also been found that due to lateral conduction and high heat transfer rates around the pin surface, pin temperatures cannot be raised adequately higher than bulk flow temperatures. Hence, we need to raise the surface temperature of the pin through internal heat generation via the use of cartridge heaters. This will be empirically proven in section 7.1. The heat generated by the cartridge heaters is assumed to be the internal heat generated within the pin. Hence, the reference volume while calculating the internal heat generated per unit volume is the pin volume. This is calculated as;

$$\dot{q} = \frac{I^2 R_{Ch}}{V_{pin}} \quad (11)$$

Here, \dot{q} is the internal heat generated per unit volume for a single pin. I is the current supplied to the individual cartridge heater. This is measured using the shunt resistor connected in series to the cartridge heaters in parallel. V_{pin} is the volume of the cylindrical pin. The current measured by the two shunt resistors (cartridge heaters in parallel + Inconel strips) is added and verified with the total current supplied & obtained from the ammeter of the Variac.

4.2 CFD- Setup and Boundary Conditions

A simple, single pin model was created in STAR-CCM+ to verify the analytical solution numerically. It should be noted that the numerical simulation was run to verify the underlying hypothesis of our analytical methodology and not to verify the accuracy of the results obtained through simulation. The hypothesis being, the pin base temperature can be used to obtain pin surface average Nusselt number. Hence, a mesh independence test was not carried out.

As a first check to verify the analytical solution obtained in Section 5, a simulation was run with a specified heat transfer coefficient on the surface of the solid aluminum pin. The parameters used were the same as the one used in our experimental setup. A constant heat transfer coefficient on the pin surface with a constant heat flux at the base, internal heat generation within the pin and an adiabatic tip were the boundary conditions imposed for this case. The purpose of this simulation was to examine the pin base temperature obtained if all the assumptions made for the analytical solution were still valid. The second step was to do a conjugate heat transfer (CHT) analysis on a single pin in an internal channel having the same parameters as the 1st case. For the CHT case, we solve both the conduction and convection equations simultaneously. The local velocities and transport variables in this case are obtained by solving the Reynold's Averaged Navier-Stokes (RANS) equations. A detailed description of the Navier-Stokes equations can be found in standard fluid mechanics reference books. The RANS approach models turbulence by averaging the unsteadiness of the turbulence. Since we average the unsteadiness of the turbulence, this method is not as resource intensive as DNS & LES. Equation (12) is the RANS equation where the fluid properties, u and p are expressed as a sum of the mean and

fluctuating components.

$$\frac{\partial(\rho\bar{u}_i)}{\partial x} + \frac{\partial(\rho\bar{u}_i\bar{u}_j + \rho\overline{u'_i u'_j})}{\partial x} = -\frac{\partial\bar{p}}{\partial x} + \frac{\delta}{\delta x_j} \left[\mu \left(\frac{\delta\bar{u}_i}{\delta x_j} + \frac{\delta\bar{u}_j}{\delta x_i} \right) \right] \quad (12)$$

The quantity $\overline{u'_i u'_j}$ is known as the Reynolds stress tensor which is symmetric and has six components. Thus, by decomposing the fluid properties into a sum of mean and fluctuating values gives rise to additional unknown quantities with no new equations. Hence, to close the system of equations, we include a few equations which are known as turbulence model equations. Previous efforts (Fernandes et al, 2015) have shown that the shear stress transport (SST) k- ω turbulence model yields the most accurate predictions of pin-fin thermal performance, as compared against experimental results and hence is the choice of turbulence model here. The two additional equations in this model which helps us close the RANS equations are given by Equations (13) & (14) below,

$$\frac{\partial k}{\partial t} + U_j \frac{\delta k}{\delta x_j} = \tau_{ij} \frac{\partial U_i}{\partial x_j} - \beta^* k \omega + \frac{\delta}{\delta x_j} \left[(v + \sigma^* v_T) \frac{\delta k}{\delta x_j} \right] \quad (13)$$

$$\frac{\partial \omega}{\partial t} + U_j \frac{\delta \omega}{\delta x_j} = \frac{\alpha \omega}{k} \tau_{ij} \frac{\partial U_i}{\partial x_j} - \beta \omega^2 + \frac{\delta}{\delta x_j} \left[(v + \sigma v_T) \frac{\delta \omega}{\delta x_j} \right] \quad (14)$$

Figure 4-11 shows the boundary conditions applied for the CHT case.

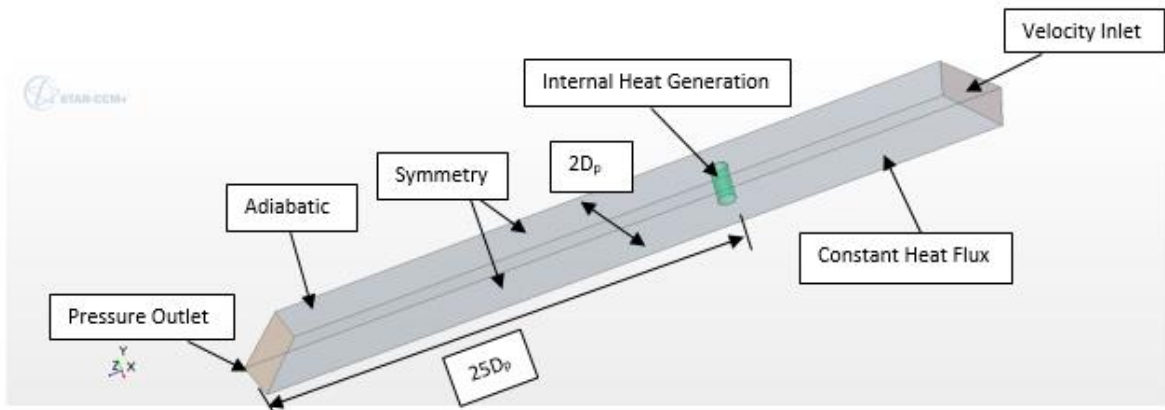


Figure 4-11. Boundary Conditions for the CHT case.

The boundary conditions are similar to the one used to obtain the analytical solution. Constant heat flux at the bottom, sidewalls were set to symmetry boundaries to mimic an infinitely wide array, constant internal heat generation within the pin, adiabatic top wall with a specified fluid velocity at the inlet and an atmospheric pressure outlet condition at the exit. The only difference being that our longitudinal conduction model assumption was violated. Sidewalls were set at a $2D$ distance, the outlet at $25D$ from the pin to ensure reflections from both boundaries didn't affect the solution at the pin surface.

The cell count was approximately 4 million cells. The mesh consisted of polyhedral cells with 10 prism layers of total thickness 1 mm, in order to resolve the boundary layer at the surface. The wall y^+ was ensured to be below 1 everywhere. This can be seen in Figure 4-12.

The simulation was run for a Reynolds number of 30,000 based on the inlet velocity and pin diameter.

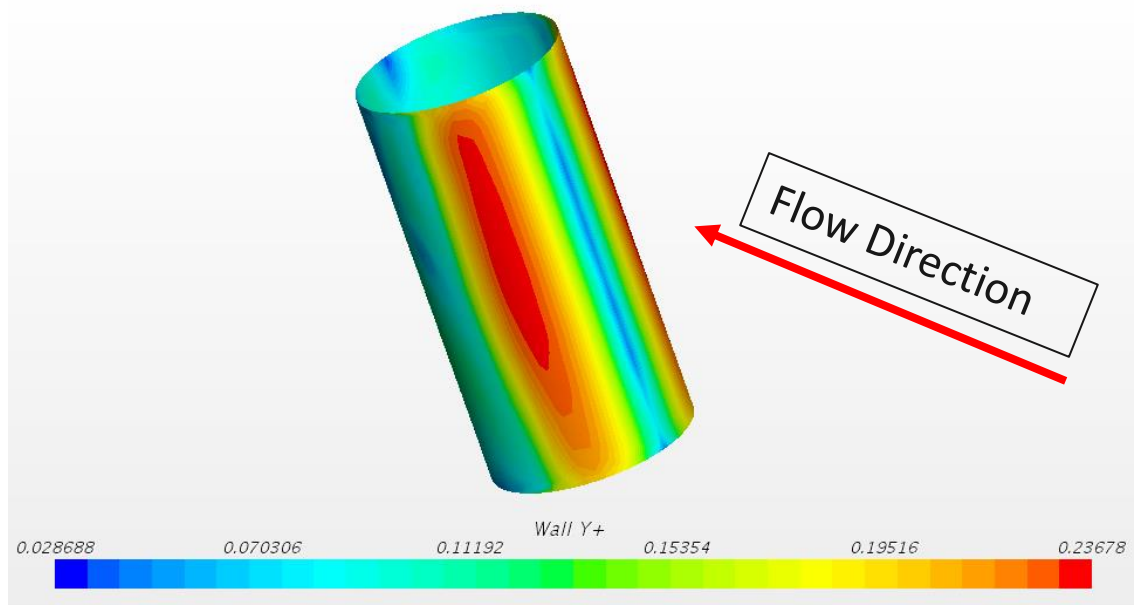


Figure 4-12. Wall y^+ for the CHT case.

5. Extended Surface Methodology (ESM)

5.1 Introduction to Extended Surface Analysis

One of the easiest and powerful methods for simplification of analysis for a pin-fin channel is the 1-D analytical model based on the extended surface theory. Using this, we can predict the surface average heat transfer coefficients on the extended surface. Figure 5-1 shows the simplest model of an extended surface of finite length L , cross-sectional area A_c , thermal conductivity k and perimeter P . The extended surface is in physical contact with a hot surface at temperature, T_{base} . Surrounding the extended surface is a fluid having heat transfer coefficient h , at temperature T_{∞} such that $T_{base} > T_{\infty}$.

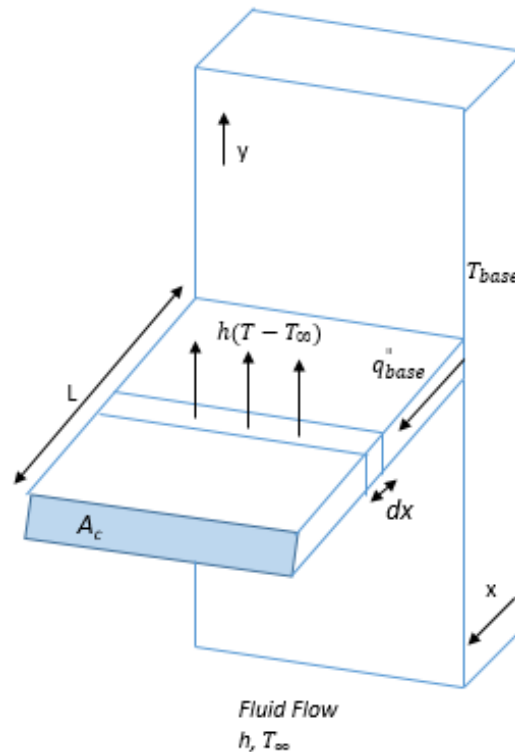


Figure 5-1. 2D Model of an extended surface.

To simplify the analysis, certain assumptions are made. Conduction is assumed to

be only in the longitudinal direction i.e. only along the fin length even though the conduction is two dimensional. However, the conduction in the lateral direction is negligible enough to be ignored. Other assumptions are steady state conditions, constant thermal conductivity, negligible radiation, no heat generation within the pin and the heat transfer co-efficient is uniform over the surface.

With these assumptions, by doing a simple energy balance over an elemental cut-section of length dx & using equations (2) and (3), we obtain this general governing equation for an extended surface,

$$\frac{d^2\theta}{dx^2} - m^2\theta = 0 \quad (15)$$

$$\text{where } m = \sqrt{\frac{hP}{kA_c}} \text{ \& } \theta(x) = T(x) - T_\infty$$

m is known as the fin parameter and θ is the excess temperature function.

A variety of analytical solutions for the modelling of extended surfaces exist depending on the boundary conditions at the tip listed in Figure 5-2, namely convective heat transfer at the tip, adiabatic tip, known tip temperature and an infinitely long fin.

Tip Condition	Temperature distribution $\frac{\theta}{\theta_{base}}$	Fin Heat Transfer q_{base}
Convective heat transfer $h\theta(L) = -k \left(\frac{d\theta}{dx} \right)_{x=L}$	$\frac{\cosh m(L-x) + \frac{h}{mk} \sinh m(L-x)}{\cosh mL + \frac{h}{mk} \sinh mL}$	$M \frac{\cosh m(L-x) + \frac{h}{mk} \sinh m(L-x)}{\cosh mL + \frac{h}{mk} \sinh mL}$
Adiabatic Tip $\left(\frac{d\theta}{dx} \right)_{x=L} = 0$	$\frac{\cosh m(L-x)}{\cosh mL}$	$M \tanh mL$
Given temperature $\theta(L) = \text{Known}$	$\frac{\frac{\theta_L}{\theta_{base}} \sinh m(L-x) + \sinh m(L-x)}{\sinh mL}$	$\frac{M \cosh mL - \frac{\theta_L}{\theta_{base}}}{\sinh mL}$
Infinitely long fin $\theta(L) = 0$	e^{-mx}	M

Figure 5-2. Analytical Solutions for different tip conditions.

An infinite fin is a fin which satisfies the parameter given by $mL \geq 4.2$ such that the temperature at the tip approaches the free stream temperature (Bejan, 2003). Application of these solutions to a pin-fin channel requires the Biot number of the pin to be much less than one. The Biot number is given by equation (16),

$$Bi = \frac{hL}{k} \quad (16)$$

In other words, the resistance due to conduction within the pin must be much less than that due to convection on the surface of the pins.

For the assumptions stated earlier but now including the effect of internal heat generation, the governing equation is as follows;

$$\frac{d^2\theta}{dx^2} - m^2\theta = -\frac{\dot{q}}{k} \quad (17)$$

where \dot{q} is the Internal heat generation within the pin. (W/m^3)

The solution (Bejan, 2003) for such a system is given for an infinitely fin as,

$$\theta(x) = \theta_b e^{-mx} + \frac{\dot{q}}{km^2} (1 - e^{-mx}) \quad (18)$$

In the next section, a solution for a finite length fin with internal heat generation is derived which is representative of our experimental setup.

5.2 Derivation of Analytical Solution

The boundary conditions for our experimental setup, as shown in Figure 5-3, can thus be stated as follows; pin of finite length, known constant heat flux at the base, insulated tip, forced convection caused by the air from the blower as well as uniform internal heat generation within the pin. We assume a 1D model for simplicity sake. All distances are measured from the base of the pin. Also, since the Biot number is expected to be less than one due to our previous experiments, the longitudinal conduction model is assumed to be valid.

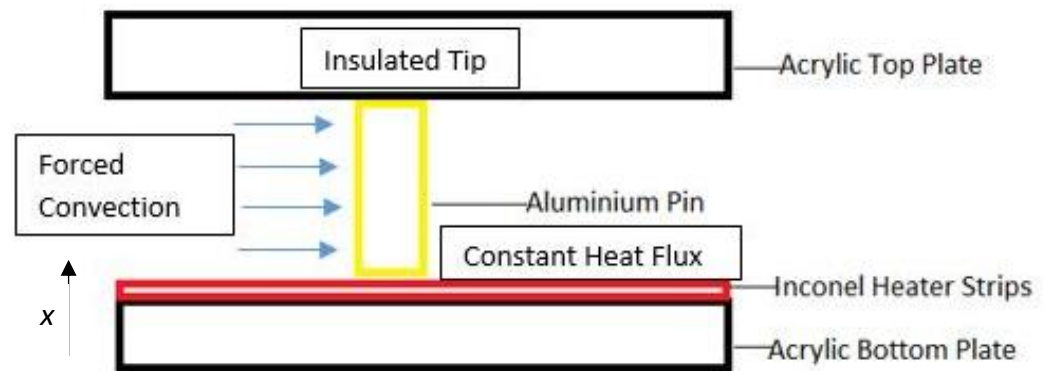


Figure 5-3. Schematic of analytical model along with boundary conditions.

The governing equation for such a system is given by equation (17). The general

solution is obtained by solving the above equation using the Method of Annihilators;

$$\theta(x) = c_1 e^{mx} + c_2 e^{-mx} + c_3 \quad (19)$$

The boundary conditions can be expressed mathematically as;

$$@ x = 0, \quad -k \frac{d\theta}{dx} = q_b'' \quad @ x = L, \quad \frac{d\theta}{dx} = 0 \quad (20)$$

Using the boundary conditions, we can solve for the constants and the solution for such a system is obtained as:

$$\theta(x) = \frac{(q_b'' \cdot e^{mx-2mL} + q_b'' \cdot e^{-mx})}{km(1-e^{-2mL})} - \frac{q}{km^2} \quad (21)$$

This gives us the temperature distribution along the length of the pin. Inversely, using an iterative method and the known values of heat flux and temperature at the base, we can calculate the surface average pin heat transfer co-efficient. The solution is later verified against equation (18) in section 6.1

6. Results & Discussion

6.1 Analytical Verification Results

To verify the analytical solution obtained in section 5.2, it was compared to the standard solution presented in heat transfer handbooks for a fin of infinite length with similar boundary conditions.(Bejan, 2003) The solution for a fin of infinite length with constant heat flux at the base is given by equation (18).

However, it should be noted that equation (18) is a solution for a pin of infinite length and hence to compare with equation (21), the current model was implemented with the condition $mL \geq 4.2$ Table 1 lists the parameters used for the comparison between the two solutions. These parameters are representative of our experimental setup.

Using the parameters listed in Table 6-1, taking the infinite length to be 0.3m , we observe that our analytical solution matches that of Bejan's exactly, as shown in Figure 6-1.

Table 6-1. Pin parameters

Pin diameter (D)	0.015 m
Actual Pin height	0.03 m
Infinite Fin Approximation height (L)	0.3 m
h	200 W/m ² -K
k (aluminum)	205 W/m-K
T_∞	300 K
q_b"	3200 W/m ²
Bi	0.00297
q̇	3.116 W/m ³

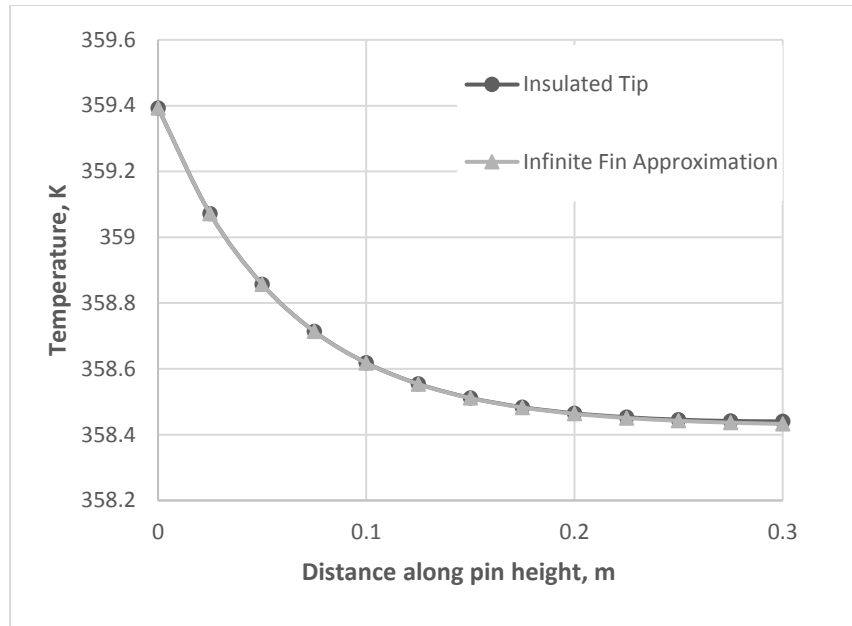


Figure 6-1. Verification of Analytical solution w/ standard solution for infinite fin.

Using the parameters listed in Table 1, and taking the pin to be of finite length, temperature distribution along the pin height was obtained with and without internal heat generation as shown in Figure 6-2 & 6-3 . We can see that with internal heat generation, the pin surface temperature is $\sim 20^{\circ}\text{C}$ higher than the free-stream temperature, with a variation of 0.3°C from the base to the pin, due to the low Biot number.

Thus, as mentioned earlier internal heat generation is necessary in order to sufficiently raise the pin surface temperatures above the freestream.

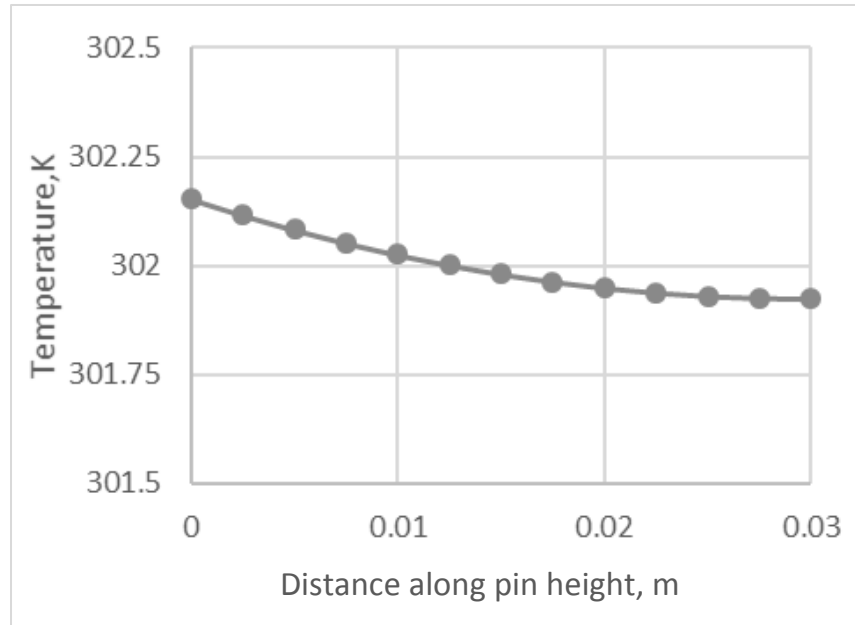


Figure 6-2. Temperature distribution along the pin height without IHG.

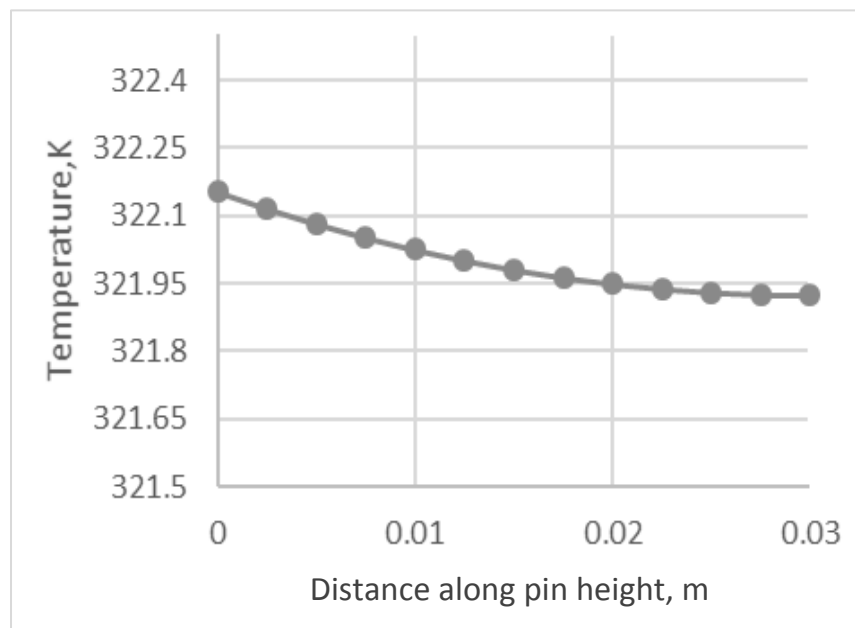


Figure 6-3. Temperature distribution along the pin height with IHG.

6.2 Computational Verification Results

First, the pin surface average Nusselt number was obtained from the simulation. Second, the average base temperature of the pin as obtained from the simulation was input into the non-linear equation (21) and solved iteratively using MATLAB® to obtain the surface average heat transfer coefficient. This heat transfer coefficient was then non-dimensionalised as the Nusselt number and compared with the value obtained from the simulation. The initial guess for the non-linear equation was obtained from the theoretical fin parameter based on previous experimentation i.e values in Table 1. It was found that the solution was not dependent on the initial guess for the non-linear equation since MATLAB® uses a Trust-region Dogleg method (MathWorks Documentation, MATLAB 2015b, 2015). More information on this method can be found in the user document.

As we can see from Table 6-2, the pin surface averaged Nusselt number obtained from our analytical methodology is in close agreement with the value obtained via CFD.

Table 6-2. Comparison with CFD

Case	Surface Average Nu		% Error
	CFD	ESM	
Prescribed Nu	103	103.18	0.1748
CHT	102.99	101.08	1.8545

6.3 Experimental Verification Results

After the numerical verification was completed, the analytical methodology was tested on a full-scale pin-fin channel. The setup of this entire rig is explained in an earlier section. However, before running tests to prove our underlying hypothesis, certain tests

were done to establish confidence in the results obtained from our measurement techniques.

6.3.1 Rig Validation- Intensity of Lights

One of the earliest tests done to validate our experimental setup was the intensity of lights test. As mentioned earlier, temperatures are determined from TSP using the intensity ratio of the reference and data image. The accuracy of the intensity captured is dependent on the stability of the light intensity emitted by the light source, UV light in this case. Readings would be consistent only if there is minimal fluctuation of intensity. Hence, it is very important to know the time taken by the light to reach a stable intensity. The point of this test was to establish a suitable “warm-up” time for the UV lights to reduce uncertainty.

Figure 6-4 shows the intensity stabilization over time for one such test.

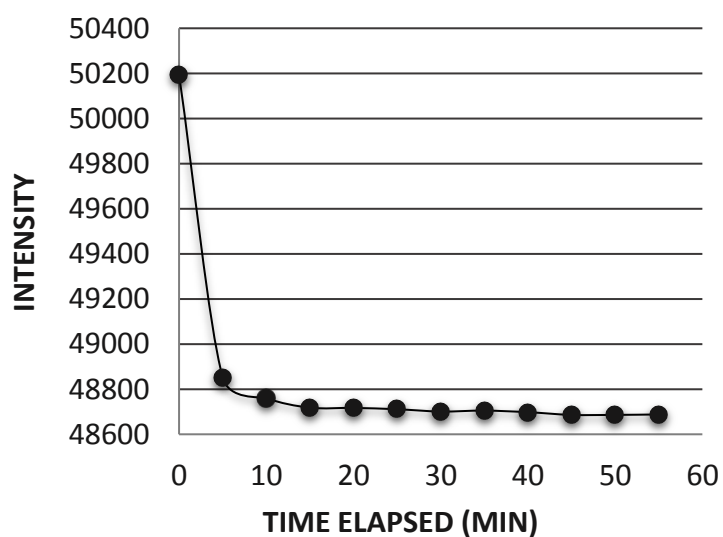


Figure 6-4. Intensity Stabilization over time

The UV light is shone upon a white paper such that it is uniformly illuminated. The

focal length and exposure time adjustments of the CMOS camera are made such that the maximum possible intensity is captured by it. Four images were captured & saved for a single time instance to average out the intensities. The overall time and the exposure time were recorded. Images were taken at 5 minute intervals. The tests were conducted for two different exposure times. As we can see from Figure 6-4, the intensity of lights stabilizes after 10 minutes and hence, the warm up time for the lights was established to be about 10 minutes.

6.3.2 Rig Validation- Heat Leakage Test

As mentioned earlier, a constant heat flux was supplied to the Inconel strips via Joule heating by varying the applied voltage using a variable AC transformer. To account for the heat lost to the surrounding by the test channel, a simple heat leak test was conducted. The test section was filled with insulating material and a low heat flux was provided to the bottom wall without any air flowing through the section. Figure 6-5 shows a schematic of the heat leak test arrangement.

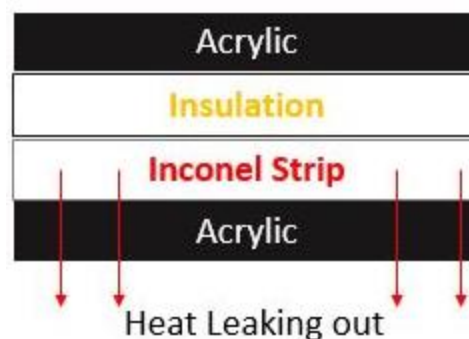


Figure 6-5. Schematic of Heat Leak Test arrangement

The tightly packed insulating material ensured that natural convection was

minimized and thus, all the heat flux provided would have only one way to escape the test channel i.e. through the acrylic bottom plate.

As shown in Figure 6-6, the heat lost to the surrounding was found to be a function of the difference in temperature between the endwall and the ambient air just outside the test section given by,

$$q_{lost}'' = 19.99 * \Delta T \quad (22)$$

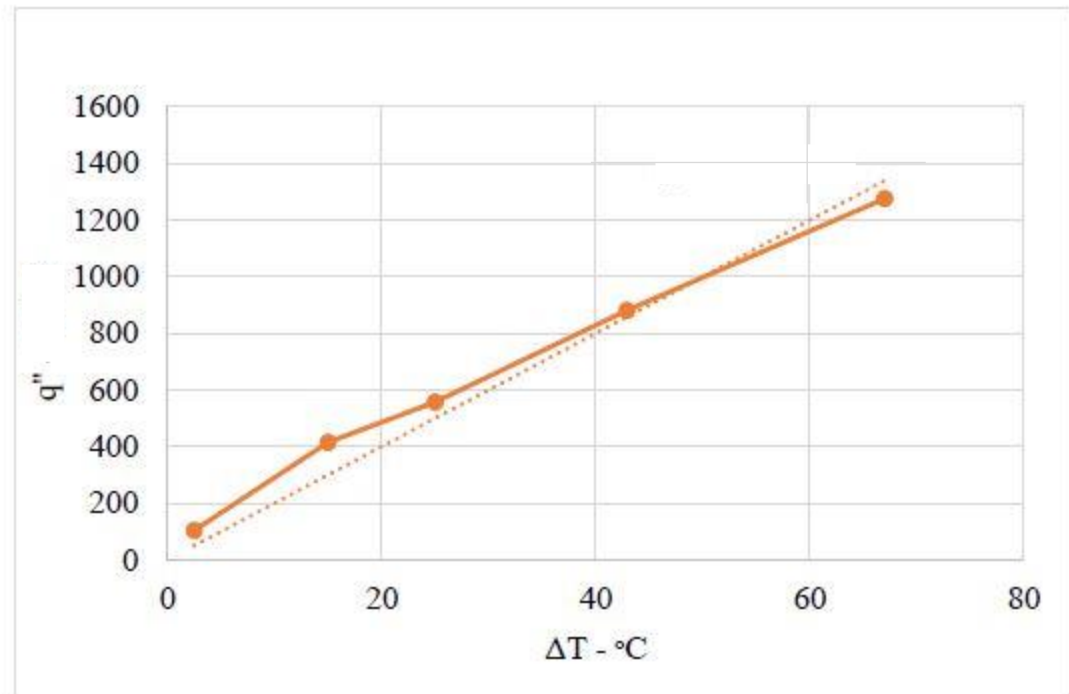


Figure 6-6. Heat Leakage Test Results- Difference in temperature vs Heat flux supplied.

6.3.3 Rig Validation- Smooth Channel Test

After the heat leakage test, a smooth channel validation was done in order to establish confidence in the heat transfer results obtained from our test rig and measurement techniques before proceeding further. A smooth channel is an internal channel without any

flow turbulators that help enhance heat transfer. The spanwise averaged Nusselt Number for the smooth channel was compared to Gnielinski's correlation for Nusselt number in a smooth channel with fully developed flow for a Reynold's number of 12,500 (Bejan, 2003) as shown in Figure 6-7.

Since heating begins at the start of the test section, the impact of thermal development of the flow is seen up to approximately at an X/D of 15. After this point, the experimental spanwise average is in agreement with Gnielinski's correlation given by equation (20), well within $\pm 12\%$ of Gnielinski's (1976) experimental uncertainty.

$$Nu = \frac{\left(\frac{f}{8}\right)(Re-1000)Pr}{1+12.7\left(\frac{f}{8}\right)^{0.5}\left(Pr^{\frac{2}{3}}-1\right)} \quad (23)$$

where f is the Darcy friction factor given by,

$$f = (0.79 \ln(Re) - 1.64)^{-2} \quad (24)$$

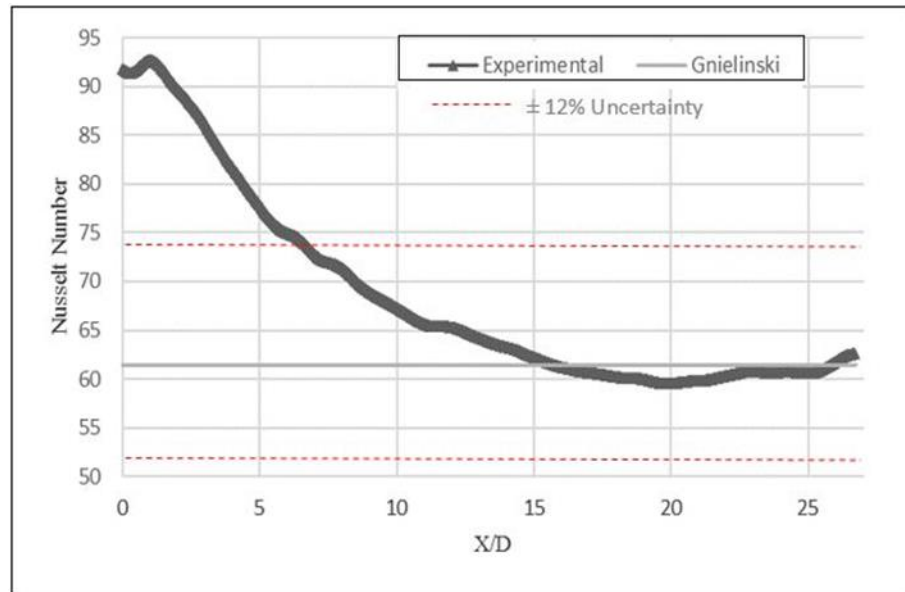


Figure 6-7. Spanwise averaged smooth channel Nusselt number.

6.3.4 ESM Results-Comparison with Ames

As mentioned earlier, Ames et al. (2006) obtained midline circumferential distribution of Nusselt number for a single pin through rows 1-5 of a staggered pin-fin array in the form of $Nu/Re^{0.5}$ for Reynolds numbers of 3,000, 10,000 and 30,000. This was accomplished by employing 24 thermocouples machined around the pin surface, equidistant from each other. This circumferential distribution was then averaged to obtain a single value of Nusselt number corresponding to each row and Reynolds number. Our experiment had cartridge heaters machined into individual pins of rows 2,4,5,7 & 8. Thus, comparison is done for pins of rows 2,4 and 5. Figure 6-8, 6-9 & 6-10 show the comparison between Ames' data and the analytical solution for the 3 cases.

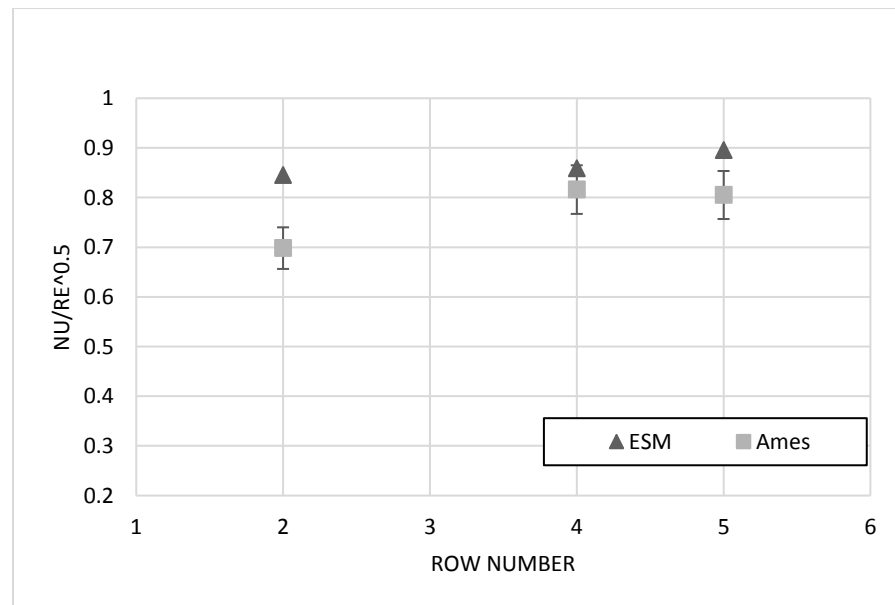


Figure 6-8. Comparison of analytical solution with Ames for $Re=3,000$.

From Figure 6-8, the highest error in pin surface averaged Nusselt number is 21% obtained for row 2. The values obtained for rows 4 and 5 are in close agreement with Ames'

data having an error of ~8% on an average.

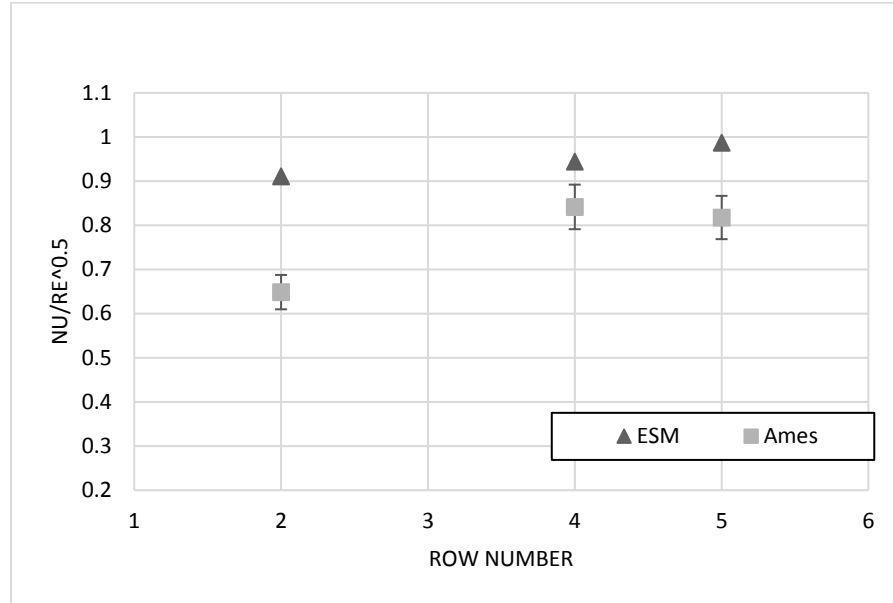


Figure 6-9. Comparison of analytical solution with Ames for Re=10,000.

Again, in Figure 6-9, we see that relatively, the highest error in surface averaged Nusselt number is for row 2 as compared to Ames' data. The percentage error for row 4 & 5 are 12% and 20% respectively.

Similar to the previous two Reynolds number cases, for Re=30,000, the highest error in the surface averaged Nusselt number is observed for row 2, while row 4 and row 5 are in close agreement (~8%) with Ames' experimental data, as can be seen in Figure 6-10.

It is fairly evident from figures 6-8, 6-9 and 6-10 that the analytical solution has the highest disagreement in row 2 for all Reynolds numbers. One of the possible reasons for this discrepancy could be that Ames' has a heated test entrance length, because of which his flow is fully developed hydro-dynamically as well as thermally. Our experimental setup does not have a heated entrance length and hence is not thermally full developed until the

second row.

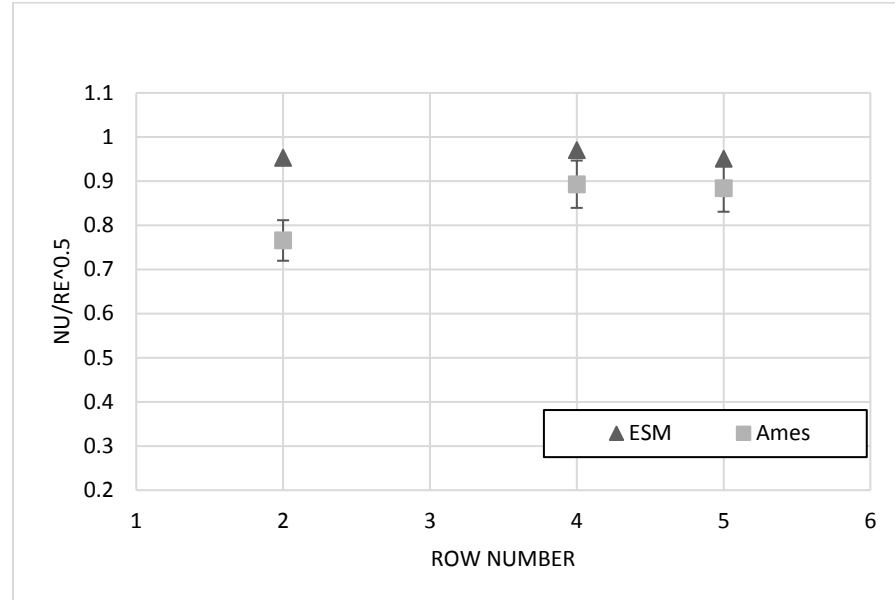


Figure 6-10. Comparison of analytical solution with Ames for Re=30,000.

6.3.5 Channel Average Nusselt number Results

The channel average Nusselt number is an average of both, pins and endwall values. Hence, endwall Nusselt numbers were also obtained for the three test cases. Then, the pins and endwall Nusselt numbers were averaged into a single value to obtain an average Nusselt number for the entire endwall and another for the pins.

Figure 6-11 is a raw image of the endwall Nusselt number contour for the Reynold's number of 30,000. The arrows indicate the regions of data that have been ignored while calculating the average endwall Nusselt number. These are regions of the through bolt washers, regions where the strips have peeled off because of delamination as well as the areas between the strips which are unheated. After repeated heated tests, the acrylic test section was found to warp in size. Since

the acrylic test section and the aluminum pins were machined to have a tight fit, warping of the test section created a gap, forcing the pins to lose contact with the Inconel strips. The through bolt and washer arrangement ensured physical contact between the pin and the strips. The smearing of data around the pin locations are a result of lateral conduction along the strips. These areas are ignored for this study but for future investigations, these can be corrected for. Areas under the pin represent the heat transfer that occurs due to the fin effect and hence have been ignored. Encircled in the same figure, in rows 2,4,5,7 & 8 are the pins with cartridge heaters machined in them. These are the pins used to compare the surface average Nusselt numbers obtained from the analytical methodology with Ames et al. (2006). The region within the dotted lines is the region considered for the averaging of endwall Nusselt number.

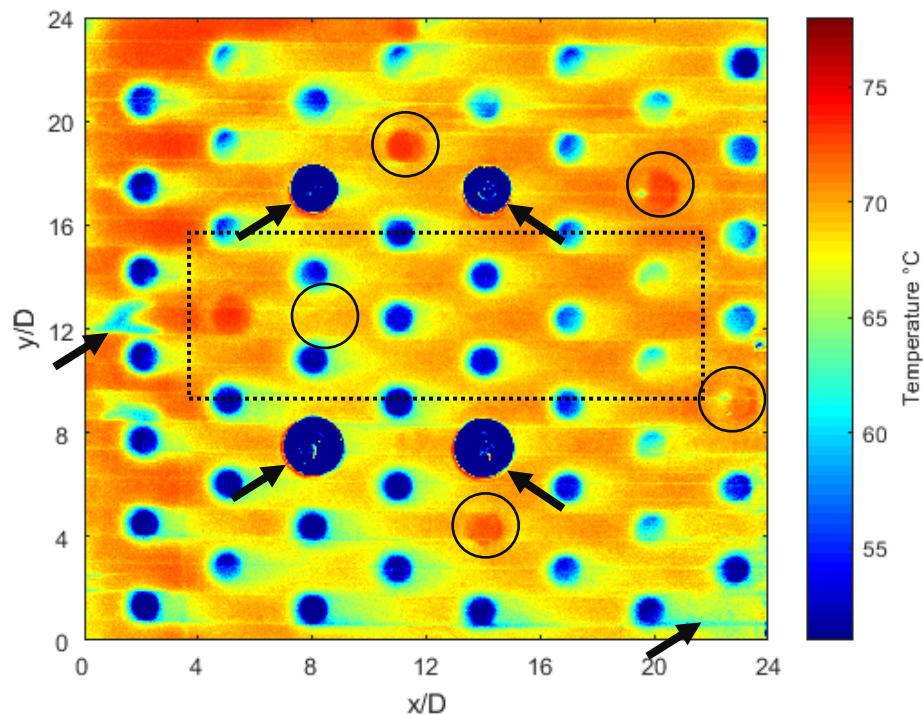


Figure 6-11. Endwall Nusselt number contour for $Re=30,000$.

Figure 6-12 is a plot of various average Nusselt numbers for the different Reynold's number cases that were run, compared to some of the previous work done by researchers. (Ames et al. (2007), Metzger et al. (1982), van Fossen(1982)) From this figure, it becomes clear that the pin surface Nusselt numbers are higher than the endwall by 40% which is consistent with previous findings (Chyu(1999), VanFossen(1981), Al Dabagh and Andrews (1992)). It should be noted that pin average Nusselt number shown in the above figure is an average of the three pins' surface average Nusselt number that were obtained using the analytical methodology in the previous section. The pin surface data from the other rows were not considered while calculating this average since the pin surface data was not collected at those rows. The author believes including that data would drive the pin Nusselt number average lower than what they are currently. The experimental pin average Nusselt number for the 3 Reynold's number cases were compared to the correlation given by VanFossen, 1981. Except for the Reynold's number case of 30,000, the average pin surface Nusselt number is higher than the value obtained by VanFossen for reasons discussed earlier. The highest difference is found for the lowest Reynold's number case.

Since the endwall has a much greater area as compared to the pin surface in totality, it would be unfair to compare the channel average by simply taking an arithmetic average of the average value of the two. The channel average Nusselt number data presented here is thus an area weighted average, weighing in the contribution of the pin and endwall based on corresponding area. From figure 6-11, we can see that the area weighted channel average of the Nusselt number is in close agreement with both Ames' and Metzger's data. On an average, the percentage difference was about 5% and 9% with Ames's and Metzger's channel average Nusselt numbers. The highest difference with Ames's data was observed

for the Reynold's number case of 30,000, about 8% while for Metzger's data it was for the low Reynold's number case having 13% difference. The uncertainty in the determination of Nusselt number for both studies were given to be $\pm 5\%$ and $\pm 6\%$ respectively.

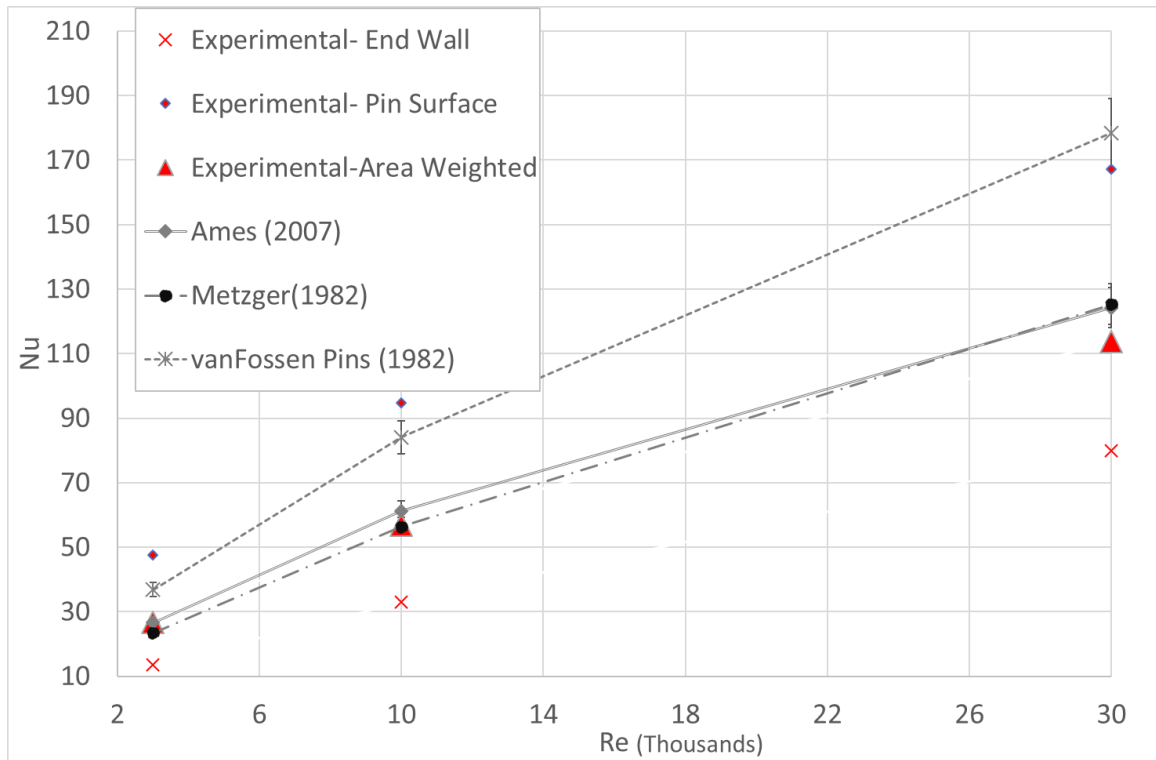


Figure 6-12. Comparison of average Nusselt numbers with previous research.

7. Conclusion

The purpose of this study was to provide a new methodology to obtain pin surface average heat transfer coefficients in pin fin cooling experimentation by using non-intrusive techniques such as TSP. This methodology was verified analytically, numerically as well as experimentally. The hypothesis was that the base temperature of the pin can be used to predict surface average heat transfer coefficients of the pins. The base temperature at the pin was determined using TSP. This helps in reducing setting up times and complexity of the experimentation at the cost of additional post processing efforts.

1. An analytical solution was obtained to do the same for the boundary conditions common to pin fin cooling experimentation as well as the in-house experimental rig. The analytical solution with a few minor modifications was verified after comparison with a standard solution listed in heat transfer reference books. The need for raising the pin surface temperature using internal heat generation via the use of cartridge heaters was also shown by the analytical solution.

2. A conceptual validation of the method using CFD was also undertaken. Two cases were run, first a conduction only case and second, a CHT case. Nusselt numbers obtained using this analytical method were found to be within 2% of the simulation results.

3. For experimental validation, a study conducted by Ames et al, was chosen for comparison. The reason being their experimental setup was similar to in house experimental setup. Pin surface average Nusselt numbers were compared for pins from

rows 2,4 & 5 for Reynold's numbers of 3,000, 10,000 & 30,000. The highest error on an average was found to be for row 2 for all Reynold's numbers of about 25%. This could be attributed to the fact that the in house experimental rig did not have a heated entrance length contrary to Ames' experiment. Nusselt numbers for row 4 and row 5 on an average, for all Reynold's numbers, showed an error of 8% and 12% respectively.

4. Endwall Nusselt numbers were also studied. The pin surface heat transfer coefficient was found to be 40% higher than endwall heat transfer coefficient. Area weighted, channel average Nusselt number versus Reynold's number was also compared and found to be in close agreement with correlations given previously by various researchers.

Thus, using just the endwall temperature measurements, Nusselt numbers were obtained for both the endwall as well as the pin surface. This aids in faster turn-around times of testing different pin geometries for gas turbine cooling.

Some of the recommendations to further this investigation is the use of rheostats for individual power control to the cartridge heaters, including the correction of lateral conduction along the Inconel strips which results in faux high heat transfer rates around the pin base and a detailed uncertainty estimation of the ESM itself.

REFERENCES

- Ames, F. E., Dvorak, L. A., & Morrow, M. J. (2004, January). Turbulent augmentation of internal convection over pins in staggered pin fin arrays. In *ASME Turbo Expo 2004: Power for Land, Sea, and Air* (pp. 787-796). American Society of Mechanical Engineers.
- Ames, F. E., & Dvorak, L. A. (2006, January). The influence of reynolds number and row position on surface pressure distributions in staggered pin fin arrays. In *ASME Turbo Expo 2006: Power for Land, Sea, and Air* (pp. 149-159). American Society of Mechanical Engineers.
- Ames, F. E., & Dvorak, L. A. (2006). Turbulent transport in pin fin arrays: experimental data and predictions. *Journal of turbomachinery*, 128(1), 71-81.
- Ames FE, Nordquist CA, Klennert LA. Endwall Heat Transfer Measurements in a Staggered Pin Fin Array With an Adiabatic Pin. ASME. Turbo Expo: Power for Land, Sea, and Air, Volume 4: Turbo Expo 2007, Parts A and B ():423-432. doi:10.1115/GT2007-27432
- Armstrong JJ, Winstanley DD. A Review of Staggered Array Pin Fin Heat Transfer for Turbine Cooling Applications. ASME. J. Turbomach. 1988;110(1):94-103. doi:10.1115/1.3262173.
- Baughn JW, Ireland PT, Jones TV, Saniei NN. A Comparison of the Transient and Heated-Coating Methods for the Measurement of Local Heat Transfer Coefficients on a Pin Fin. ASME. Turbo Expo: Power for Land, Sea, and Air, Volume 4: Heat Transfer; Electric Power; Industrial and Cogeneration ():V004T09A031. doi:10.1115/88-GT-180.
- Bejan, A., & Kraus, A. D. (2003). Heat transfer handbook (Vol. 1). John Wiley & Sons.
- Bell, James, Schairer, E., Hand, L., Mehta, R. (2001). "Surface Preassure Measurements Using Luminescent Coatings". *Journal of Fluid Mechanics*, 33, pp 155-206.
- Bernard L. Koff, "Gas Turbine Technology Evolution: A Designer's Perspective", Turbo Vision, Inc., Palm Beach Gardens, Florida, 2004.
- Brigham, B. A., & Van Fossen, G. J. (1984). Length to diameter ratio and row number effects in short pin fin heat transfer. *ASME, Transactions, Journal of Engineering for Gas Turbines and Power* (ISSN 0022-0825), 106, 241-245.
- Boyce M. P. (2006), Gas Turbine Engineering Handbook, 3rd Edition.
- Chang, S. W., Yang, T. L., Huang, C. C., & Chiang, K. F. (2008). Endwall heat transfer

and pressure drop in rectangular channels with attached and detached circular pin-fin array. *International Journal of Heat and Mass Transfer*, 51(21), 5247-5259.

Chyu MK, Hsing YC, Natarajan VV. Convective Heat Transfer of Cubic Fin Arrays in a Narrow Channel. ASME. Turbo Expo: Power for Land, Sea, and Air, Volume 4: Heat Transfer; Electric Power; Industrial and Cogeneration ():V004T09A020. doi:10.1115/96-GT-201.

Chyu MK, Hsing YC, Shih TP, Natarajan VV. Heat Transfer Contributions of Pins and Endwall in Pin-Fin Arrays: Effects of Thermal Boundary Condition Modeling. ASME. Turbo Expo: Power for Land, Sea, and Air, Volume 4: Heat Transfer; Electric Power; Industrial and Cogeneration ():V004T09A037. doi:10.1115/98-GT-175.

Chyu, M. K., Hsing, Y. C., Shih, T. P., & Natarajan, V. (1999). Heat transfer contributions of pins and endwall in pin-fin arrays: effects of thermal boundary condition modeling. *Journal of Turbomachinery*, 121(2), 257-263.

Clarke, D. R., Oechsner, M., & Padture, N. P. (2012). Thermal-barrier coatings for more efficient gas-turbine engines. *MRS bulletin*, 37(10), 891-898.

Clifford, R. J. (1985, September). Rotating heat transfer investigations on a multi-pass cooling geometry. In In AGARD Heat Transfer and Cooling in Gas Turbines 12 p (SEE N86-29823 21-07).

Dabagh A, Andrews GE. Pin-Fin Heat Transfer: Contribution of the Wall and the Pin to the Overall Heat Transfer. ASME. Turbo Expo: Power for Land, Sea, and Air, Volume 4: Heat Transfer; Electric Power; Industrial and Cogeneration ():V004T09A022. doi:10.1115/92-GT-242.

Downs, J. P., and Landis, K. K., "Turbine Cooling Systems Design - Past, Present and Future", Jupiter, FL: Florida Turbine Technologies, Inc., 2009

Fernandes, R. (2016). Investigation of Pin Fin Cooling Channels for Applications in Gas Turbines.

Fernandes, R., Ricklick, M., and Pai, Y., 2015, "CFD Benchmarking of Heat Transfer and Pressure Drop Predictions in a Pin Fin Channel." 51st AIAA/SAE/ASEE Joint Propulsion Conference, AIAA Propulsion and Energy Forum, (AIAA 2015-3736)

Gavrieli, K., Salim, N. Yanez, A. (2004) Jet Engine, A Historical Introduction
<http://cs.stanford.edu/people/eroberts/courses/ww2/projects/jetairplanes/how.html>

Gnielinski, V. (1976). New equations for heat and mass-transfer in turbulent pipe and channel flow. *International chemical engineering*, 16(2), 359-368.

- Goldstein, R. J., Jabbari, M. Y., & Chen, S. B. (1994). Convective mass transfer and pressure loss characteristics of staggered short pin-fin arrays. *International Journal of Heat and Mass Transfer*, 37, 149-160.
- Han, J. C. (2004). Recent studies in turbine blade cooling. *International Journal of Rotating Machinery*, 10(6), 443-457.
- Han, J. C., Dutta, S., & Ekkad, S. (2012). *Gas turbine heat transfer and cooling technology*. CRC Press.
- Hanke, W., Witte, M., Miersch, L., Brede, M., Oeffner, J., Michael, M., & Dehnhardt, G. (2010). Harbor seal vibrissa morphology suppresses vortex-induced vibrations. *The Journal of experimental biology*, 213(15), 2665-2672.
- Hwang, J. J., & Lui, C. C. (2002). Measurement of endwall heat transfer and pressure drop in a pin-fin wedge duct. *International Journal of Heat and Mass Transfer*, 45(4), 877-889.
- Incropera, F. P., & De Witt, D. P. (1985). *Fundamentals of heat and mass transfer*.
- Kirsch KL, Ostanek JK, Thole KA, Kaufman E. Row Removal Heat Transfer Study for Pin Fin Arrays. ASME. Turbo Expo: Power for Land, Sea, and Air, Volume 5A: Heat Transfer ():V05AT12A006. doi:10.1115/GT2014-25348..
- Lawson, Seth A., Alan A. Thrift, Karen A. Thole, and Atul Kohli. 2011. "Heat transfer from multiple row arrays of low aspect ratio pin fins." *International Journal of Heat and Mass Transfer* 54, (17): 4099-4109
- Lei, Z. (2005). Effect of RANS turbulence models on computation of vortical flow over wing-body configuration. *Transactions of the Japan Society for Aeronautical and Space Sciences*, 48(161), 152-160.
- Liu, Quan, Kapat, J, "Study of Heat Transfer Characteristics of Impinging Air Jet Using Pressure and Temperature Sensitive Luminescent Paint", UCF Dissertation, May 2006.
- Liu, T., Campbell, B., Sullivan, J. (1995). "Accuracy of TSP for heat transfer measurements". AIAA 95-2042.
- MathWorks Documentation, MATLAB 2015b (2015) <http://www.mathworks.com/help/signal/ref/butter.html>
- Meher-Homji, C. B., Zachary, J., & Bromley, A. F. (2010, October). Gas Turbine Fuels-System Design, Combustion and Operability. In *Proceedings of the 39th*

Turbomachinery Symposium, George R. Brown Convention Center, Houston, Texas (pp. 4-7).

- Metzger DE, Haley SW. Heat Transfer Experiments and Flow Visualization for Arrays of Short Pin Fins. ASME. Turbo Expo: Power for Land, Sea, and Air, Volume 4: Heat Transfer; Electric Power ():V004T09A007. doi:10.1115/82-GT-138.
- Morris, W. D., & Chang, S. W. (1997). An experimental study of heat transfer in a simulated turbine blade cooling passage. *International Journal of Heat and Mass Transfer*, 40(15), 3703-3716.
- Muktinutalapati, N. R. (2011). Materials for Gas Turbines-An Overview. INTECH Open Access Publisher.
- Nguyen, T. D., & Harmand, S. (2013). Heat transfer and vortical structures around a rotating cylinder with a spanwise disk and low-velocity crossflow. *International Journal of Heat and Mass Transfer*, 64, 1014-1030.
- Pai, Y., Prasad, A., Fernandes, R., Ricklick, M., (2017). Bio-Inspired Cylinders for Enhanced Heat Transfer in Internal Cooling of Gas Turbines, AIAA Propulsion & Energy Forum, 2017, Atlanta, GA.
- Peles, Y., Koşar, A., Mishra, C., Kuo, C. J., & Schneider, B. (2005). Forced convective heat transfer across a pin fin micro heat sink. *International Journal of Heat and Mass Transfer*, 48(17), 3615-3627.
- Prasad, A., & Ricklick, M. A. (2017). A Detailed Uncertainty Analysis of Heat Transfer Experiments using Temperature Sensitive Paint. In 55th AIAA Aerospace Sciences Meeting (p. 1283).
- Ricklick, M. A., & Carpenter, C. (2014). Comparison of Heat Transfer Prediction for Various Turbulence Models in a Pin Fin Channel. 50th AIAA/ASME/SAE/ASEE Joint Propulsion Conference, AIAA Propulsion and Energy Forum, (AIAA 2014-3838)
- Sahiti, N., Lemouedda, A., Stojkovic, D., Durst, F., & Franz, E. (2006). Performance comparison of pin fin in-duct flow arrays with various pin cross-sections. *Applied Thermal Engineering*, 26(11), 1176-1192.
- Sautner, M., Clouser, S., Han, J.C., 1992. "Determination of Surface Heat Transfer and Film Cooling Effectiveness in Unsteady Wake Flow Conditions." AGARD Conference Proceedings 527, pp. 6-1 to 6-12.
- Shyam, V., Ameri, A., Poinatte, P., Thurman, D., Wroblewski, A., & Snyder, C. (2015, June). Application of Pinniped Vibrissae to Aeropropulsion. In *ASME Turbo Expo 2015: Turbine Technical Conference and Exposition* (pp. V02AT38A023-V02AT38A023). American Society of Mechanical Engineers.

- Siw, S. C., Chyu, M. K., Shih, T. I. P., & Alvin, M. A. (2012). Effects of pin detached space on heat transfer and pin-fin arrays. *Journal of Heat Transfer*, 134(8), 081902.
- Sparrow, E. M., Ramsey, J. W., & Altemani, C. A. C. (1980). Experiments on in-line pin fin arrays and performance comparisons with staggered arrays. *ASME J. Heat Transfer*, 102(1), 44-50.
- Sparrow, E. M., & Molki, M. (1982). Effect of a missing cylinder on heat transfer and fluid flow in an array of cylinders in cross-flow. *International journal of heat and mass transfer*, 25(4), 449-456.
- Sparrow, E. M., Stahl, T. J., and Traub, P., 1984, Heat Transfer Adjacent to the Attached End of a Cylinder in Crossflow," *International Journal of Heat and Mass Transfer*, Vol. 27, pp. 233-242.
- Sparrow, E. M., Abraham, J. P., & Tong, J. C. (2004). Archival correlations for average heat transfer coefficients for non-circular and circular cylinders and for spheres in cross-flow. *International Journal of Heat and Mass Transfer*, 47(24), 5285-5296.
- Uzol, O., & Camci, C. (2005). Heat transfer, pressure loss and flow field measurements downstream of staggered two-row circular and elliptical pin fin arrays. *Journal of heat transfer*, 127(5), 458-471.
- VanFossen, G. J. (1982). Heat-transfer coefficients for staggered arrays of short pin fins. *Journal of Engineering for Power*, 104(2), 268-274.
- Wiberg, R., & Lior, N. (2004). Errors in thermochromic liquid crystal thermometry. *Review of scientific instruments*, 75(9), 2985-2994.
- Zukauskas, A., & Ziugzda, J. (1985). Heat transfer of a cylinder in crossflow. Washington, DC, Hemisphere Publishing Corp., 1985, 219 p. Translation., 1